Faculty of Postgraduate Studies and Scientific Research

German University in Cairo

Development of a Magnetic Tracking System for Microrobots and Magnetic Rendering Applications

A thesis submitted in partial fulfillment of the requirements for the degree of Master of Science in Mechatronics Engineering

By

Mohanad Ahmed Mansour

Supervised by

Dr. Islam Khalil

Associate Professor

Faculty of Material Science and Engineering

German University in Cairo

2019

ACKNOWLEDGMENTS

First, I would like to convey my sincere gratitude and appreciation to my advisor Dr. Islam Khalil for the planning of this work and for his patience, motivation, constant supervision and immense knowledge, his office door was always open whenever I ran into a trouble or had a question about my research or writing.

My sincere gratefulness also goes to the MNR lab family, Alaaeldine Adel, Mina Maged, Dalia Mahdy, and Ahmed Hassan for great support, for the sleepless nights we were working together before deadlines, and for all the fun we have had throughout the entire process.

Last but not the least, I would like to thank my family for providing me with unfailing support and continuous encouragement. This accomplishment would not have been possible without them. Thank you.

TABLE OF CONTENTS

Page

LIST OF FIGURES

Figure Page

Figure Page

Figure Page

Figure Page

Figure Page

ABSTRACT

Magnetic tracking has developed a significant research interest in the field of biomedical engineering. However, the presence of undesired background magnetic field increases the complexity of the tracking process. It is essential to minimize the effect of the background magnetic field in order to achieve high tracking accuracy. This work presents magnetic tracking techniques using magnetic field sensors to determine the position of a permanent magnet under the influence of background magnetic field. In order to eliminate the background field, pre-calculated magnetic field map and extra array of magnetic field sensors are used. Magnetic tracking is implemented in two applications. First, localization and control of helical microrobots during removal of superficial blood clots inside *in vitro* and *ex vivo* models. Pre-calculated magnetic field map is used to minimize the effect of background field generated by the actuation system of the robot on the tracking system. The tracking accuracy is validated using visual feature tracking inside *in vitro* model with mean absolute position error of 2.5 ± 0.4 mm ($n = 15$). Magnetic tracking is used to localize the robot inside a rabbit aorta and whole blood as *ex vivo* models and the localization accuracy is validated using ultrasound feedback with mean absolute position error of 2.6 mm. Second, localization of a wearable magnetic dipole during the interaction with an Electromagnetic-Based haptic interface. Two identical arrays of magnetic field sensors are used to exploit the symmetry of the haptic interface for a model-free background field elimination. Tracking of the dipole is validated under 4 background field conditions: Absent, constant, periodic variable and random variable. Experimental results show that the system can achieve a mean absolute error of 0.962 ± 0.34 mm ($n = 500$). The difference between the presented technique and modeling the background field is investigated.

1. INTRODUCTION

Object tracking and localization have attracted a considerable interest in many applications, as it can be used in exploration of space [1] down to nano particles [2]. Tracking is the estimation of the position of an object either within a coordinate system, or relative to a known position over time. Determination of the position of an object (Fig. 1.1) is essential for achieving navigation and control, or studying the behavior of the tracked object, and even exploration of the surrounding environment. There are various techniques for tracking an object such as visual feedback [3], magnetic [4, 5], ultrasound feedback [6–8], inertial-based tracking [9], and hybrid tracking systems which combine the use of different techniques to compensate for the shortcomings of individual systems [10, 11]. The choice of the most suitable technique depends mainly on the application, the properties of the tracked object, and the surrounding environment. In this work, the magnetic tracking technique is implemented for tracking of microrobots and a permanent magnet used in magnetic rendering applications.

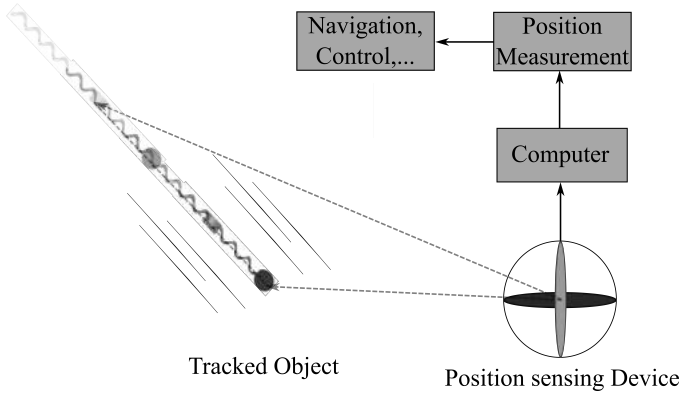

Fig. 1.1. Tracking of an object is essential for achieving navigation, control or studying the behavior of the tracked object.

1.1 Magnetic Tracking

Magnetic tracking is a relevant technique for determining the position of objects continuously. The principle of magnetic tracking depends mainly on the use of two devices, one acts as a field generator and the other acts as a sensor [4]. The magnetic field source induces voltage on the magnetic field sensor which makes the sensor able to measure the magnetic flux density of the source. The induced voltage is a function of distance and orientation of the magnetic field source. Therefore, determination of position and/or orientation of the magnetic source depending on its measured magnetic flux density is possible by finding characteristic features of the source by observing or measuring the fields caused by this source.

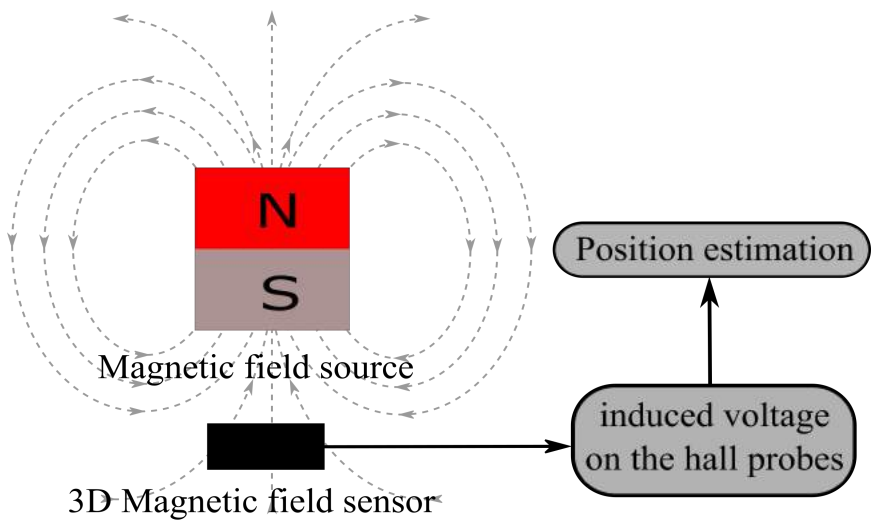

Fig. 1.2. Magnetic field source induces voltage on the hall probes of magnetic field sensor. This voltage is a function of the position of the source.

As three-dimensional (3D) Magnetic field sensors can detect 3D linear and rotation movements of a magnetic source. Therefore, it can be used in various applications such as medical or clinical applications. Popek *et al.* have implemented simultaneous localization and propulsion of a magnetic capsule in a lumen using a single rotating

dipole field. They have designed an extended Kalman filter to estimate position and orientation of the capsule as it is synchronized with the applied magnetic field [12]. Six magnetic field sensors have been embedded into a magnetic capsule with 42 mm in length to achieve simultaneous localization. Magnetically actuated shape deformation and recovery to localize a magnetically actuated soft capsule endoscope between rolling locomotion cycles have been deployed in [13]. Son *et al.* have demonstrated a five-degrees-of-freedom localization method for a meso-scale ($6.4 \times 6.4 \times 12.8$ mm^3) magnetic robot [14]. Human eye magnetic tracking for the diagnosis of neurologic, ophthalmologic, and vestibular disorders was demonstrated in [15], real time organ positioning during radiotherapy of cancer tumors [16], isolated words recognition in silent speech by patients who have lost their larynx [17]. Obviously, magnetic tracking is promising in the field of biomedical engineering due to the transparency of the human body to low frequency and/or static magnetic field.

Magnetic tracking also have various applications in virtual/augmented reality field [18]. For instance, Berkelman *et al.* have presented an electromagnetic position sensing for a fingertip-mounted magnet [19]. They have introduced a planar array of magnetometer sensors to detect the position of the magnet in order to implement haptic feedback forces that can be directly physically felt by the user. Baldi *et al.* have introduced a sensing glove based on magnetic and inertial sensors for hand tracking which is used for rendering force feedback [20].

Magnetic tracking systems can track sources with static or dynamic magnetic fields. In case of static magnetic fields the source can be a permanent magnet, on the other hand, in case of dynamic magnetic field tracking, electromagnetic coils can be used as the magnetic field source. The Tracking system can be developed by integrating the magnetic field sensor inside the tracked object which will be exposed to a field due to coils or permanent magnets, or the technique can be reversed by tracking the source of magnetic field with several sensors externally (Fig. 1.2). The reversed technique is implemented in this work, as the tracked objects include a magnetic field source which is either very small in size or affects the existence of an external magnetic field.

1.2 Biological Inspired Microrobots

Microrobots are robots designed and fabricated from components which are to the scale of a micrometer. Therefore, microrobots have potential for performing very difficult tasks on the micro scale in various medical applications [21]. Microrobots used in medical applications inside human body are usually inspired biologically from living microorganisms to have the same behavior as shown in Fig. 1.3 [22].

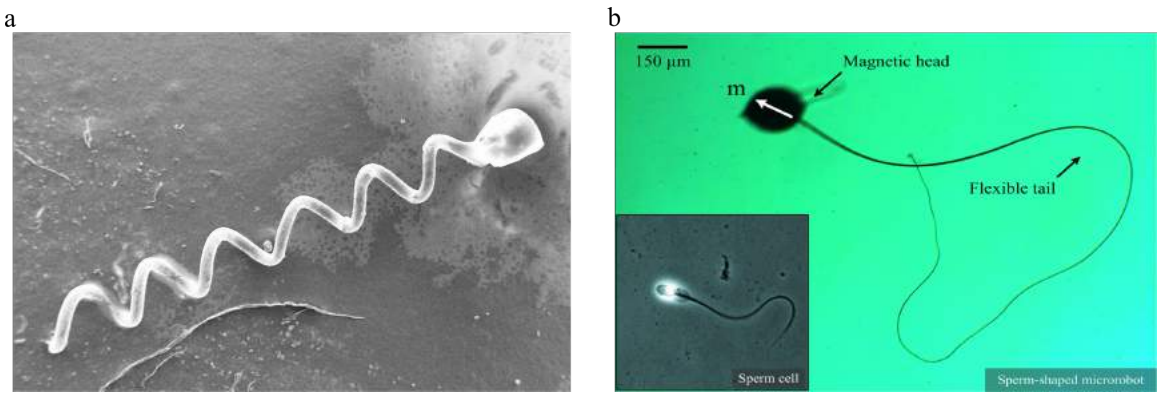

Fig. 1.3. Examples of microrobots used in medical applications. (a) Helical microrobot inspired from bacterial flagella [23]. (b) A sperm-shaped microrobot consists of a microbead and an ultra-fine fiber that resemble the morphology of a sperm cell [22].

Microrobots have to be actuated wirelessly [24–27] in medical applications due the limitation of its size, so it is not viable to carry power sources and actuating motors. Therefore, it is important to include a magnetic material in the fabrication of microrobots to acheive locomotion by applying either forces or torques to the magnetic material by external magnetic field.

Feedback control allows microrobots to compensate position error between actual and planned positions [28]. Tracking algorithms can be used to compute the trajectory of a microrobot in order to implement a feedback controller that modifies the input to the actuating system to compensate the position error during the navigation of the robot as shown in Fig. 1.4. The precision of the control of microrobots with high

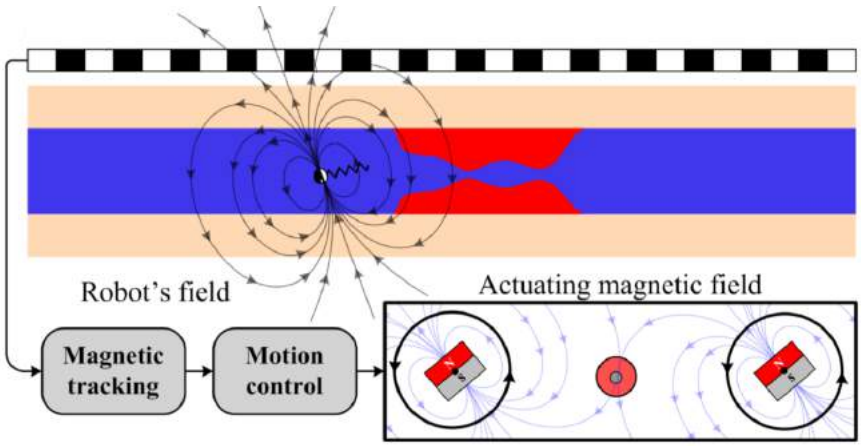

Fig. 1.4. Magnetic tracking and motion control of helical microrobot for clearing of blood clots [29].

sensitivity is extremely important to complete tasks. Therefore, computing position of the robot accurately is important, as controlling microrobots is hard to accomplish without information of its position and a small control error could cause high output errors, which may cause failures during tasks execution. Also determination of the position of the robot allows studying its behavior while performing critical tasks in medical applications. 3D magnetic field sensors can be used to detect the magnetic flux density from the magnetic materials inserted in the microrobots and therefore, the position and orientation of the microrobot can be estimated.

1.3 Magnetic Rendering

Exploring physical environments can be achieved using haptic feedback systems, allowing the user to interact with the environment at a distance, as the direct contact with this environment might be undesirable. Rendering of a physical environment holds promise in several applications as medical training simulations [30], education and video game industry by providing a haptic feedback of this environment which can be attained by various methods such as wearable haptic devices [31–33], air vor-

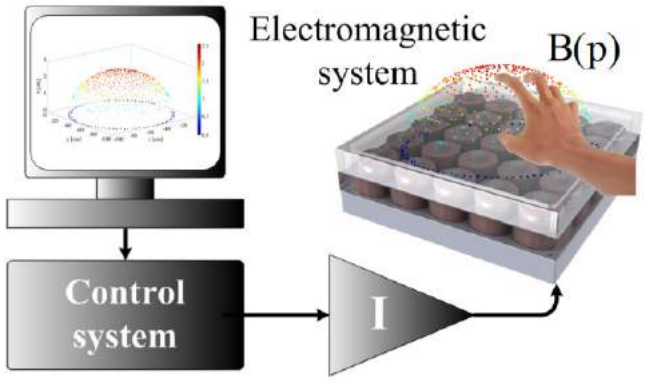

Fig. 1.5. Magnetic rendering of virtual environments using controlled magnetic forces by controlling the input current to the electromagnetic coils based on morphology of the rendered object. The input current allows the electromagnetic coils to produce magnetic field $\mathbf{B(p)}$ and magnetic field gradients to exert magnetic force on a dipole attached to a finger splint at a certain position $\mathbf{p}$ [40].

.

tex [34, 35], acoustic radiation pressure can be generated using airborne ultrasound transducers to provide forces at a distance [36, 37], and magnetic force [38–41]. Rendering virtual environments using electromagnetic systems (Fig. 1.5) mainly depends on exerting magnetic force and magnetic torque on a dipole. The generated magnetic forces can be controlled by controlling the input current to the electromagnetic coils and therefore, 3D objects in mid-air can be created using the generated magnetic fields. The dipole that the magnetic forces are exerted on can be fixed on a finger splint [41], or attached to an interaction stylus [42] to make the user able to sense the feedback force from the system.

It is significant to have information about the position of the user finger, as the optimal technique for haptic feedback is when the provided forces from the haptic device is a function of the displacement made by the user. Adel *et al.* have investigated the effect of position feedback in the rendering process and the results showed

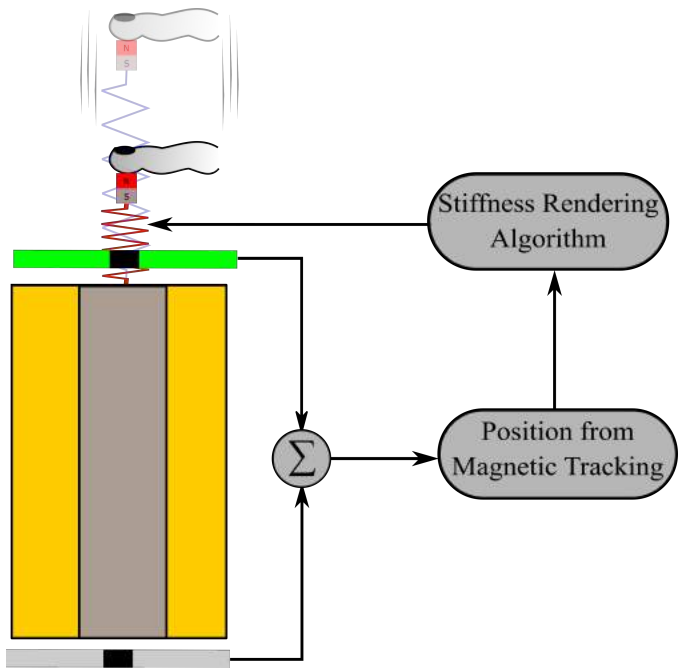

Fig. 1.6. The position feedback from a magnetic tracking algorithm can provide stiffness rendering from a force-feedback haptic device, as stiffness is a relation between the applied force and the displacement produced by this force.

that rendering virtual objects with position feedback improves the resolution of the virtual object [41]. Position feedback in electromagnetic haptic devices is important as the electromagnetic coils can experience overheating, this problem can be avoided if the coils just produce magnetic fields if the user finger is in the boundaries of the rendered object. Rendering the stiffness of an object (Fig. 1.6) is an advantage of the use of position feedback as the stiffness is a relation between the applied force and the displacement produced by this force, so with position feedback and controllable magnetic force a desired stiffness can be rendered.

2. MAGNETIC TRACKING OF MICROROBOTS

In this chapter, localization and control of a helical microrobot during clearing of superficial blood clots will be discussed. The helical robot is actuated using two rotating dipole fields [43] and localized while swimming and clearing blood clots using an array of magnetic field sensors [29].

2.1 System Description

The system consists of *in vitro* and *ex vivo* models of a blood clot, permanent magnet based robotic system, array of magnetic field sensors (Fig. 2.1). The *in vitro* model consists of a polyvinyl chloride catheter segment with inner-diameter of 4 mm filled with phosphate buffered saline (PBS), with viscosity of 0.00088 Pa.s. which is injected in the catheter segment at flow rate of 10 ml/hr using a dual syringe pump(Genie Plus, GT-4201D-12, Kent Scientific, Connecticut,USA). Motion of the helical robot is tracked with a highspeed camera (avA100-120kc, Basler Area Scan Camera, Basler AG, Ahrensburg, Germany) in order to validate the magnetic tracking accuracy. A segment from a rabbit aorta is isolated and connected to the catheter in the *ex vivo* model. A catheter segment filled with whole blood which is injected at flow rate of 10 ml/hr is also presented as an *ex vivo* model. Magnetic tracking validation in *ex vivo* is achieved using ultrasound transducer (LA523 linear array ultrasound transducer, Esaote, Italy). A helical robot (diameter of 1 mm) is also inserted and allowed to swim towards the clot against the flowing streams of the PBS. The robot is actuated using two synchronized rotating dipole fields. These fields are generated using permanent NdFeB magnets with diameter of 20 mm and length of 20 mm, and axial magnetization. Each magnet is attached to a DC motor (2322 980, Maxon Motor, Sachseln, Switzerland). The angular positions of these motors

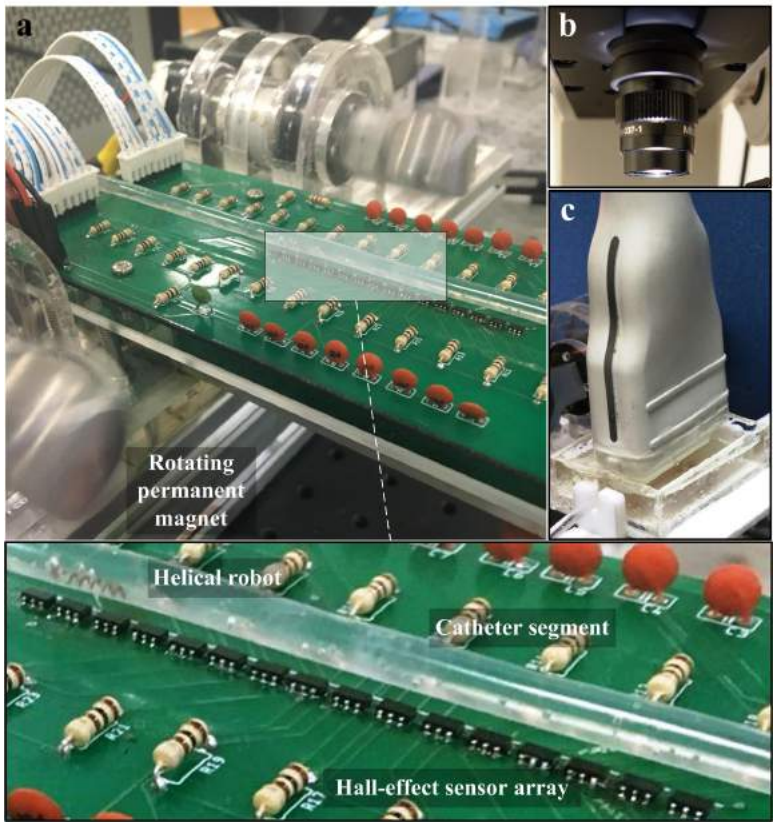

Fig. 2.1. A permanent magnet-based robotic system enables a helical robot to swim using rotating magnetic fields. (a) A catheter segment is aligned with an array of Magnetic field sensors. Position of the helical robot inside the catheter segment is estimated using measurements of these sensors. (b) Position of the helical robot is measured with a high-speed camera to validate the magnetic tracking. (c) An ultrasound transducer localizes the helical robot inside the *ex vivo* model.

are synchronized to increase the magnetic field and mitigate the magnetic force along the lateral direction of the robot. A linear array of 16 magnetic field sensors is fixed below the catheter segment, at maximum hight of 5 mm. The distance between the adjacent sensors is 1 mm. The sensitivity of these sensor is 0.1 mT within a range of $\pm$ 130 mT.

2.2 Magnetic Tracking of the Helical Robot

The helical robot consists of a cylindrical permanent magnet with magnetic moment vector ($\mathbf{m}$) perpendicular to its helix axis. A magnetic torque is applied using two dipole fields $\mathbf{B}_1$ and $\mathbf{B}_2$ as shown in Fig. 2.2. These fields are generated using two rotating permanent magnets with dipole moment $\mathbf{M}_1$ and $\mathbf{M}_2$

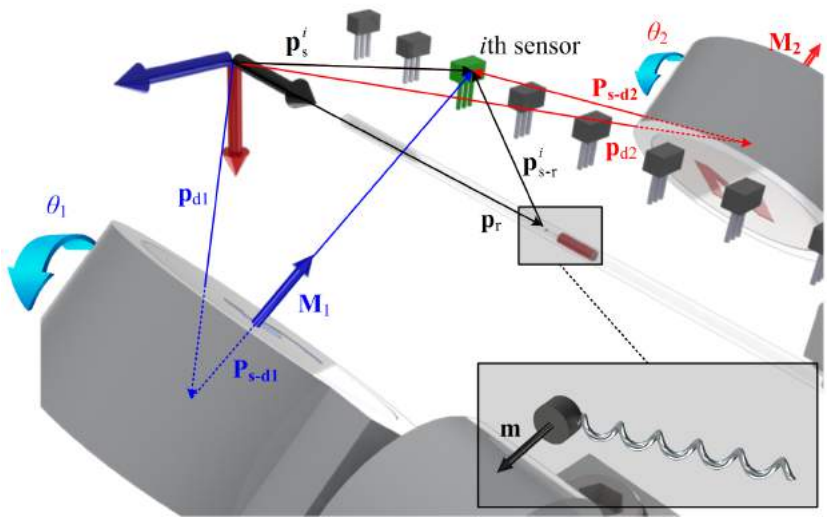

Fig. 2.2. Dipole models of the helical robot (shown magnified) and the two rotating permanent magnets are used to localize the helical robot. The helical robot (with magnetic moment $\mathbf{m}$) is contained inside a catheter segment between the two rotating permanent magnets with magnetic moment $\mathbf{M}_1$ and $\mathbf{M}_2$. $\mathbf{p}_s^i$ is position vector to the ith sensor from a reference frame and $\mathbf{p}_{s-r}^i$ is position vector to the ith sensor from the robot frame of reference. $\mathbf{p}_{d1}$ and $\mathbf{p}_{d2}$ are position vectors to the first and second rotating permanent magnets from the reference frame, respectively.

Therefore, the ith magnetic field sensor is subject to the following magnetic fields:

$$\mathbf{B}_s^i = \mathbf{B}_r + \mathbf{B}_{d1} + \mathbf{B}_{d2}, \tag{2.1}$$

where $\mathbf{B}_s^i$ is the magnetic field at the ith sensor due to the helical robot and the rotating dipoles, and $\mathbf{B}_r$ is the magnetic field of the helical robot. $\mathbf{B}_{d1}$ and $\mathbf{B}_{d2}$ are

the fields of the first and second dipole fields at the ith sensor. The magnetic field of the helical robot is given by:

$$\mathbf{B}_r = \frac{\mu_0 \mid \mathbf{m} \mid}{4\pi}\left(\frac{3(\widehat{\mathbf{m}} \cdot \mathbf{p}^i_{s-r})\mathbf{p}^i_{s-r} - \mid \mathbf{p}^i_{s-r} \mid^2 \widehat{\mathbf{m}}}{\mid \mathbf{p}^i_{s-r} \mid^5}\right), \tag{2.2}$$

where μ_0 is the magnetic permeability of free space and $\widehat{\mathbf{m}}$ is the unit vector of the magnetic moment vector of the helical robot. Further, $\mathbf{p}^i_{s-r}$ is position vector to the ith sensor from the helical robot frame of reference [4]. In (2.1), the magnetic field of the first and second rotating permanent magnets are calculated using the following equation:

$$\mathbf{B}_{dj} = \frac{\mu_0 \mid \mathbf{M}_j \mid}{4\pi}\left(\frac{3(\widehat{\mathbf{M}}_j \cdot \mathbf{p}_{dj})\mathbf{p}_{dj} - \mid \mathbf{p}_{dj} \mid^2 \widehat{\mathbf{M}}_j}{\mid \mathbf{p}_{dj} \mid^5}\right), \tag{2.3}$$

where $\mathbf{M}_j$, for $j = 1, 2$, is the magnetic moment of the jth permanent magnets and $\widehat{\mathbf{M}}_j$ is its unit vector. Further, $\mathbf{p}_{dj}$ is position vector to the ith sensor from the jth permanent magnet.

To ensure the detection of the helical robot by the magnetic field sensors a MATLAB simulation was made to simulate the magnetic field of the two rotating dipoles and the magnetic field of the helical robot at different positions: (0,25,0), (0,0,0), (0,-25,0), using equations (2.2) and (2.3) using the following parameters:

Subsystem	**Property**	**Value**
Helical Robot	Type	NdFeB
	$\mathbf{m}$ [A.m^2]	1.7×10^{-4}
	Diameter [mm]	1
	Length [mm]	4
Rotating Dipoles	Distance[mm]	150
	$\mathbf{M}_{1,2}$ [A.m^2]	6.087
	ω [Hz]	5
	Field [mT]	20

The fields are calculated at the plane of the magnetic field sensors (z = 3 mm), and for zero angular position of the rotating permanent magnets. Fig. 2.3 show the

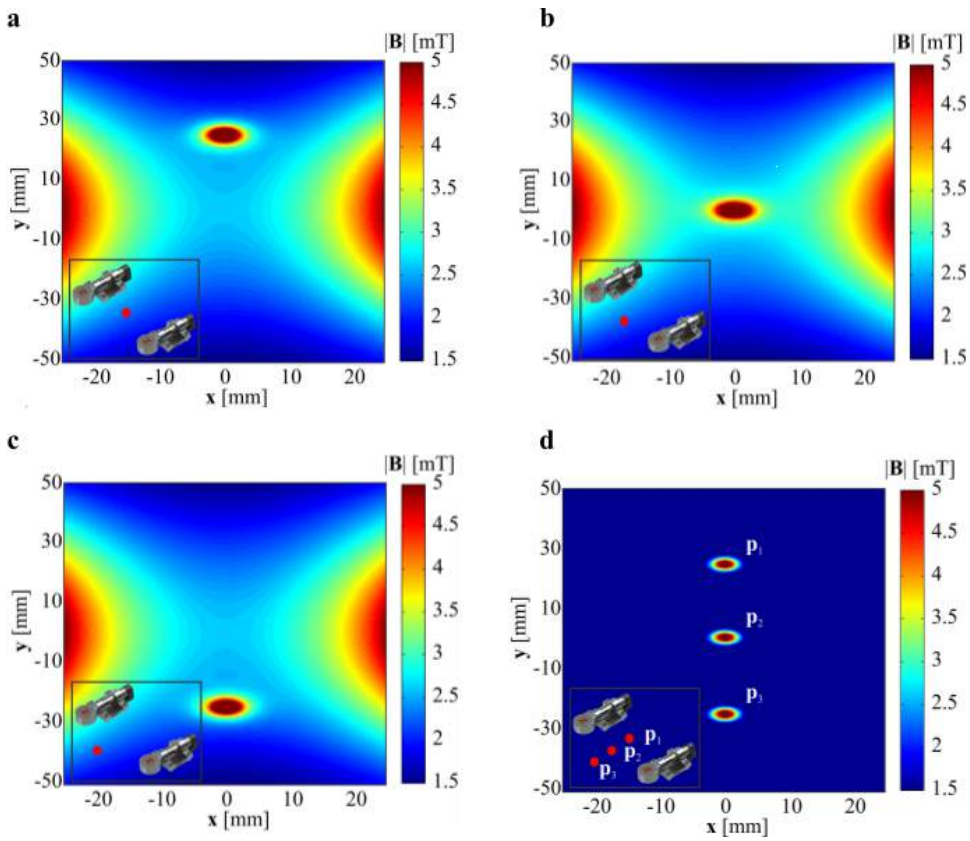

Fig. 2.3. The pre-calculated magnetic field map of the two rotating permanent magnets (zero angular position) is superimposed to the helical robots magnetic field and calculated at the plane of the Hall-effect sensor (x,y,3) mm. (a) The helical robot is positioned at (0, 25, 0) mm. (b) The helical robot is positioned at (0, 0, 0) mm. (c) The helical robot is positioned at (0, -25, 0) mm. (d) The actuating magnetic field is subtracted from the total magnetic field to provide the helical robots field at position (0, 25, 0) mm, (0, 0, 0) mm, and (0, 25, 0) mm, respectively.

simulation results and indicates that the resultant magnetic field is approximately 5 mT at the position of the sensor. The Simulation Results also indicates the magnetic field of the robot, at (z = 3 mm) for the three mentioned positions after subtraction of the actuating magnetic field. The magnetic field at the position of the sensor is one order of magnitude greater than it's sensitivity. The red dot in Fig. 2.3 indicates the position of the helical robot between the rotating dipole fields. In order to calculate

the position of the helical robot using equation (2.2), magnetic fields $\mathbf{B}_{d1}$ and $\mathbf{B}_{d2}$ are calculated using equation (2.3) , and the magnetic field $\mathbf{B}_s^i$ in equation (2.1) is measured at the ith sensor. The position vector $\mathbf{p}_s^i$ to the ith sensor from a frame of reference is fixed. Therefore, position vector of the helical robot is calculated using the following equation:

$$\mathbf{p}_r = \mathbf{p}_s^i - \mathbf{p}_{s-r}^i, \tag{2.4}$$

where $\mathbf{p}_r$ is position vector to the helical robot from a frame of reference, as shown in Fig.2.2, and $\mathbf{p}_{s-r}^i$ is solved such that the following objective function is minimized:

$$\begin{aligned} \underset{\mathbf{p}_{s-r}^i}{\text{minimize}} \quad & \epsilon = (\widehat{\mathbf{B}}_r - \mathbf{B}_r)^T (\widehat{\mathbf{B}}_r - \mathbf{B}_r) \\ \text{subject to} \quad & \begin{cases} x_{min} \leq x \leq x_{max}, \\ y_{min} \leq y \leq y_{max}, \\ z_{min} \leq z \leq z_{max}, \end{cases} \end{aligned} \tag{2.5}$$

where $\widehat{\mathbf{B}}_r$ is the calculated magnetic field using equation (2.2), and $\mathbf{B}_r$ is determined using equation (2.1) based on the magnetic field measurement and the calculated actuating magnetic fields using (2.3). Further, x, y and z are the components of $\mathbf{p}_{s-r}^i$, and their minimum and maximum values are determined based on the sensitivity of the magnetic field sensor. This optimization routine is solved iteratively using interior-method for constrained non-linear optimization using C++, and a 15-point moving average filter is used for smoothing the estimated position. The filtered position is provided to a closed-loop motion control system.

2.3 Closed-Loop Motion Control of the Helical Robot

Two DC motors are used to rotate the permanent magnets to actuate the helical robot and allow it to rotate and swim in the center of distance between the two magnetic dipoles. The DC motors have to be synchronized in order to achieve pure magnetic torque on the dipole of the helical robot without any magnetic forces,

therefore, the following control input is applied to synchronize the two rotating dipole fields:

$$u_1 = k_1(\theta_1 - \theta_2) + k_2(\omega_1 - \omega_2), \tag{2.6}$$

where k_1 and k_2 are the proportional and derivative positive gains, respectively, θ_1 and θ_2 are the angular positions of the first and second motors, ω_1 and ω_2 are the angular velocities of the first and second motors. Finally, the motion of the helical robot is controlled using the following control input:

$$u_2 = k_3(\mid \mathbf{p}_c \mid - \mid \mathbf{p}_r \mid) + k_4(\mid \dot{\mathbf{p}}_c \mid - \mid \dot{\mathbf{p}}_r \mid), \tag{2.7}$$

where k_3 and k_4 are positive proportional and derivative gains, and $\mathbf{p}_c$ is the position vector of the blood clot (desired position), $\mathbf{p}_r$ is the position of the helical robot which is calculated using equation (2.4) and used in the closed-loop motion control.

2.4 Experimental Results of Motion Control and Clearing of Blood Clots

In order to examine the validation of the magnetic tracking, the helical robot is allowed to swim inside *in vitro* and *ex vivo* models and magnetic localization is implemented.

2.4.1 Localization and Motion Control *In Vitro*

The helical robot is allowed to swim inside a catheter segment under the influence of a rotating magnetic field at frequency of 5 Hz, as shown in Fig. 2.4(a). The measured magnetic field using the magnetic field sensors and the pre-calculated magnetic field map are used in the objective function in equation (2.5) to calculate $\mathbf{p}^i_{s-r}$. The magnetic field measurements during the movement of the helical robot are shown in Fig. 2.4(b). Each magnetic field sensor provides a maximum magnetic field measurement when the robot is close to its tip. The maximum magnetic field is measured was 4.5 mT, whereas the minimum field measured by two adjacent sensors was 1.6 mT during the movement of the robot with respect to the sensors. Although the

catheter segment is aligned with the linear array of the magnetic field sensors, the peak provided by each sensor is different because of the nonuniform swimming speed of the helical robot. The helical robot is actuated using two rotating dipole fields with constant frequency of 5 Hz. However, there exist a nonuniform magnetic force along the propulsion axis as shown in Fig. 2.3(a)-2.3(c). This force contributes to the time-varying speed of the helical robot at constant frequency from the actuation system, and deviation between the peaks of adjacent sensors measurements. Position of the helical robot is tracked using visual feedback [44] to validate the magnetic tracking, as shown in Fig. 2.4(c). In this representative experiment, the mean absolute position error is 2.32 mm.

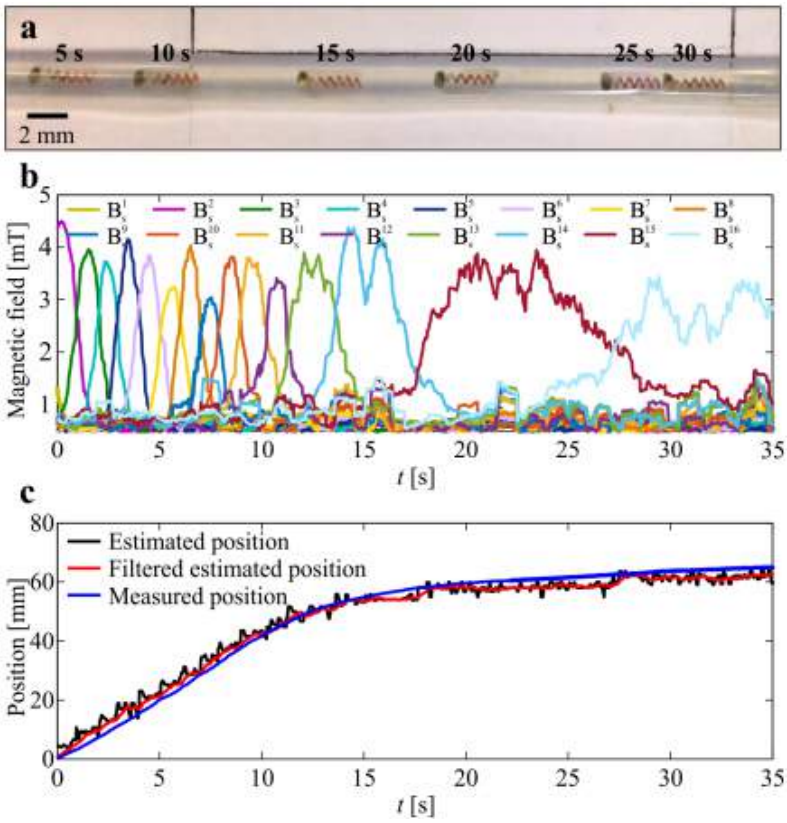

Fig. 2.4. Position of a helical robot is tracked continuously during propulsion along a catheter segment. (a) The helical robot swims under the influence of a rotating magnetic field at frequency of 5 Hz. (b) Magnetic field is measured using an array of 16 magnetic field sensors. $\mathbf{B}_s^i$ is the magnetic field measured at the ith sensor. (c) The estimated position (filtered using 15-point moving average filter) of the helical robot is compared to the measured position using computer vision. The mean absolute position error is 2.32 mm.

This experiment was repeated 15 times and the mean absolute error was calculated as 2.5 ± 0.4. This localization error is due to the signal-to-noise ratio (SNR). The SNR decreases as the distance between the helical robot and magnetic field sensor increases. In addition, deviations between the applied magnetic field and the pre-calculated magnetic field map also contributes to the localization error of the helical robot. To determine the deviation between the pre-calculated magnetic field map and applied magnetic field, the magnetic field is measured using the 16 magnetic

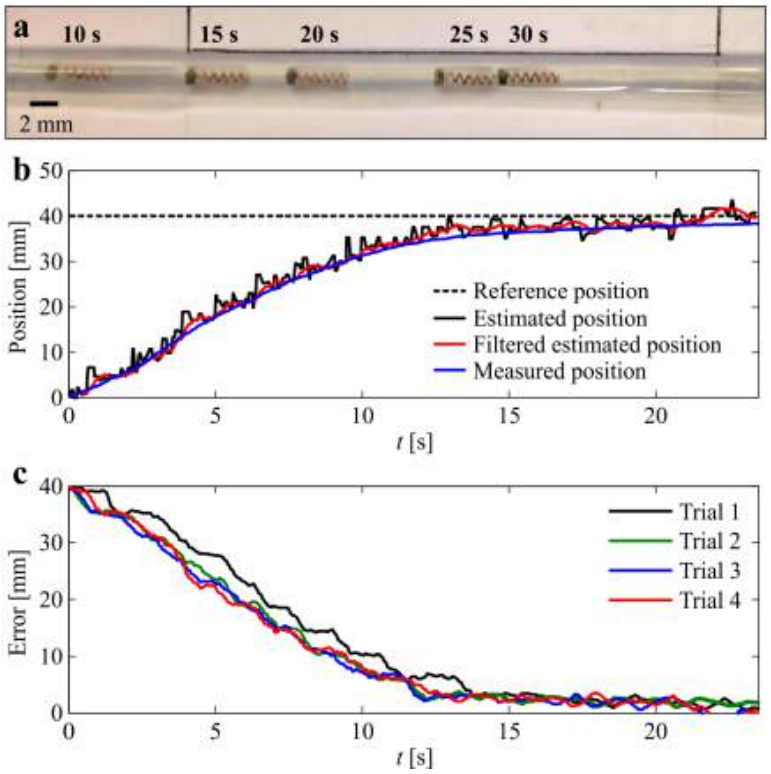

Fig. 2.5. Closed-loop motion control of a helical robot is achieved inside *in vitro* model. (a) The helical robot swims towards a reference position inside a catheter segment. (b) The estimated position (filtered using 15-point moving average filter) of the helical robot is used in the closed-loop motion control (2.7). (c) The average position steady state error is 0.74 ± 1.9 mm.

field sensors in the absence of the helical robot. The measured magnetic fields are subtracted from the pre-calculated magnetic field map. The average error is 0.67 ± 0.09 mT. Therefore, the localization performance can be improved with accurate field modeling and higher SNR using magnetic field sensors with higher sensitivity.

The calculated position of the helical robot was used in equation (2.7) to achieve closed-loop motion control, as shown in Fig. 2.5. The helical robot is positioned at the reference (dashed black line). This experiment was repeated 5 times and the average steady state error was calculated as 0.74 ± 1.9 mm.

2.4.2 Clearing of Blood Clots

1-hour-old blood clot samples were prepared and inserted inside the catheter segment. The initial volume (ν_0) of the clot is 94.24 mm^3, the diameter and length of the blood clot are 7.5 mm and 4 mm, respectively. The volume of the blood clot is measured throughout each trial via visual feedback [45–47]. Fig. 2.6 shows a representative experimental result of clearing a blood clot under the influence of a rotating magnetic field at frequency of 5 Hz. Position of the helical robot was estimated using magnetic tracking method. Although this experiment is done inside a catheter segment, visibility of the helical robot is relatively low as shown. the magnetic-based localization provides an estimate of the position of the helical robot along the catheter throughout the clearing procedure of the blood clot. The closed-loop control achieved a rise time of 7 seconds (time to reach the blood clot). Once the helical robot comes into contact with the clot, it does not move forward and its tip tears the fibrin network of the blood clot. After approximately 1.5 minutes, the helical robot penetrated the clot with depth of 3 mm. A similar behavior was observed at time, t = 10 minutes. At time t = 47 minutes, the clot was cleared and the robot was pushed back by the flowing streams of the PBS. The size of the blood clot was decreased by 60.8% and 79.7% after 40 minutes and 75 minutes of mechanical rubbing, respectively.

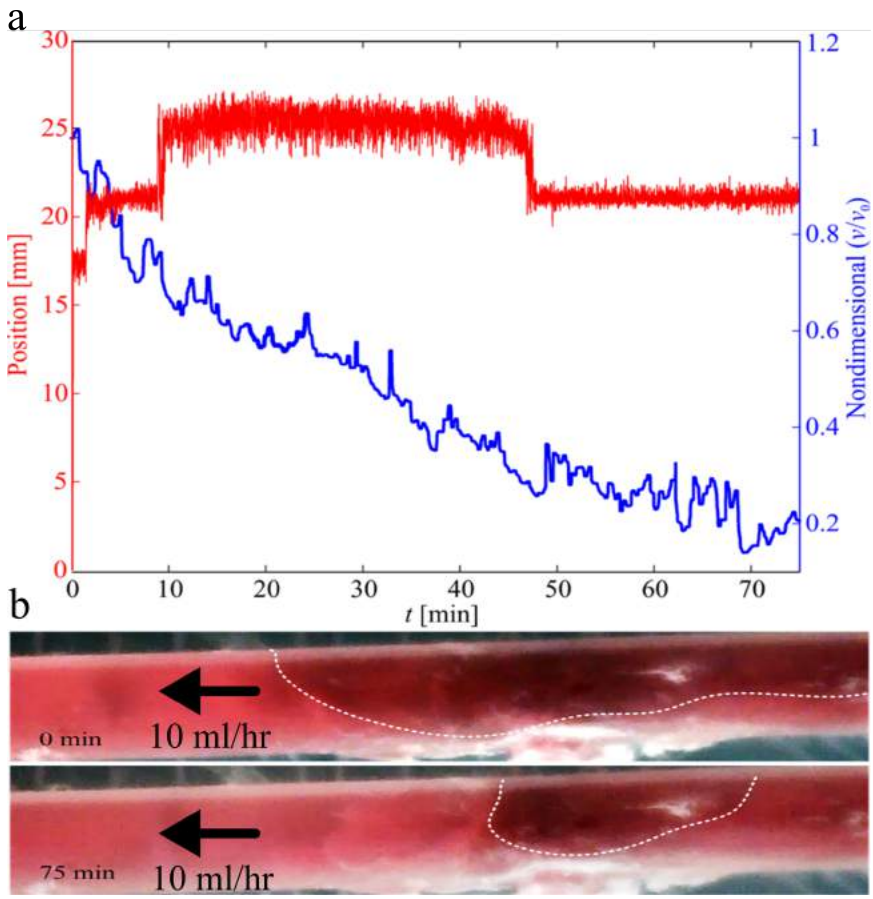

Fig. 2.6. 1-hour-old blood clot was mechanically removed using a helical robot. The robot was controlled towards the clot and mechanical removal was achieved at actuation frequency of 5 Hz, and against flow rate of 10 ml/hr. (a) Position of the helical robot was estimated using magnetic tracking and used in the motion control system. The initial volume of the clot (ν_0) is 94.24 mm^3. The size of the clot (ν) was decreased by 60.8% and 79.7% after 40 minutes and 75 minutes of mechanical rubbing, respectively.

2.4.3 Magnetic Localization *Ex Vivo*

A segment from the aorta of a rabbit was used as an *ex vivo* model in order to characterize the magnetic localization in a real blood vessel. The aorta is connected to a catheter segment to provide a constant flow rate of PBS (10 ml/hr), which is greater than blood flow in small arteriole, capillaries, and venule only. Aorta is the

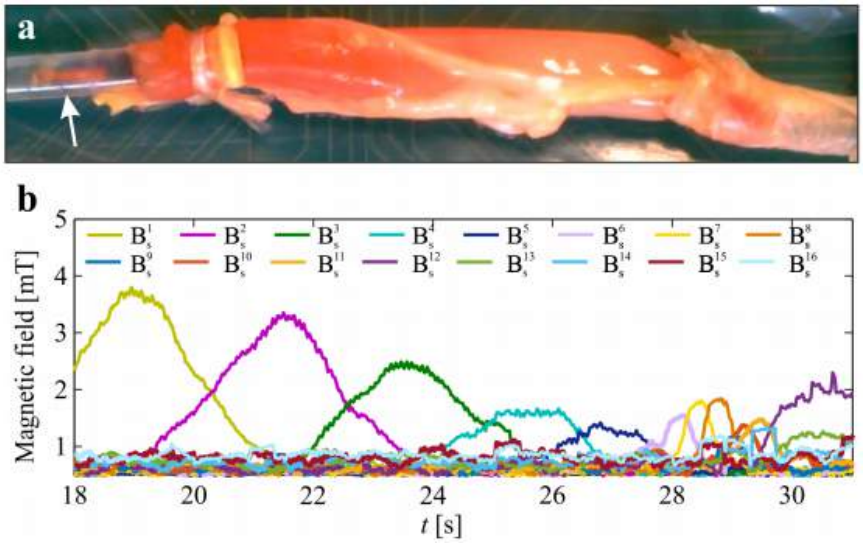

Fig. 2.7. Magnetic field sensors are used to track the helical robot inside rabbit aorta as an *ex vivo* model. (a) The helical robot swims to the aorta at an average speed of 4.4 mm/s. (b) Measured magnetic field using an array of 16 magnetic field sensors.

main artery that originates in the heart and delivers oxygenated blood to the organs. The diameter of the extracted rabbit aorta fits with the catheter segment used to deliver the flow and the use of arteries is clinically relevant, since the major cause of ischemic diseases such as stroke and myocardial infarction, is the obstruction of the corresponding artery by blood clots.

Magnetic field sensors array detects the magnetic field of the helical robot's head while it is swimming through the rabbit aorta and the position of the robot is calculated during a representative open-loop trial under the influence of a rotating magnetic field at frequency of 5 Hz. Fig. 2.7 shows the results of this representative trial which the average speed of the helical robot is 4.4 mm/s against flow rate of 10 ml/hr. This experiment was repeated 5 times (Fig. 2.8) inside the aorta and the average speed of the helical robot was measured as 7.1 $\pm$ 3.4 mm/s.

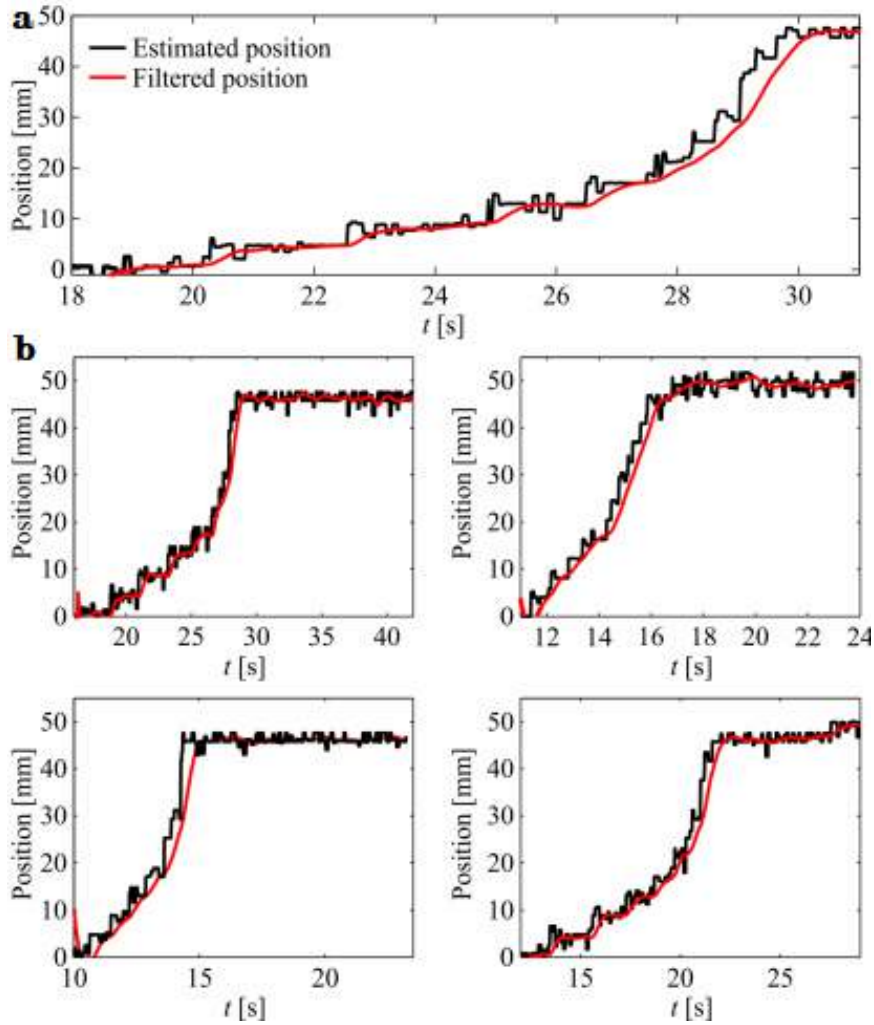

Fig. 2.8. Position of the helical robot is tracked continuously during propulsion inside a rabbit aorta. (a) The position of the helical robot during the representative trial. (b) The average speed of the helical robot inside the aorta is 7.1 ± 3.4 mm/s.

The helical robot was also allowed to swim inside a catheter segment filled with streams of whole blood with flow rate of 10 ml/hr as an *ex vivo* model. The position of the helical robot was calculated while swimming in the whole blood using the 16 magnetic field sensor array and the accuracy of the magnetic tracking was validated using an ultrasound transducer. The catheter segment is filled with whole blood and contained in a gelatin reservoir to achieve air-free coupling with the transducer. The

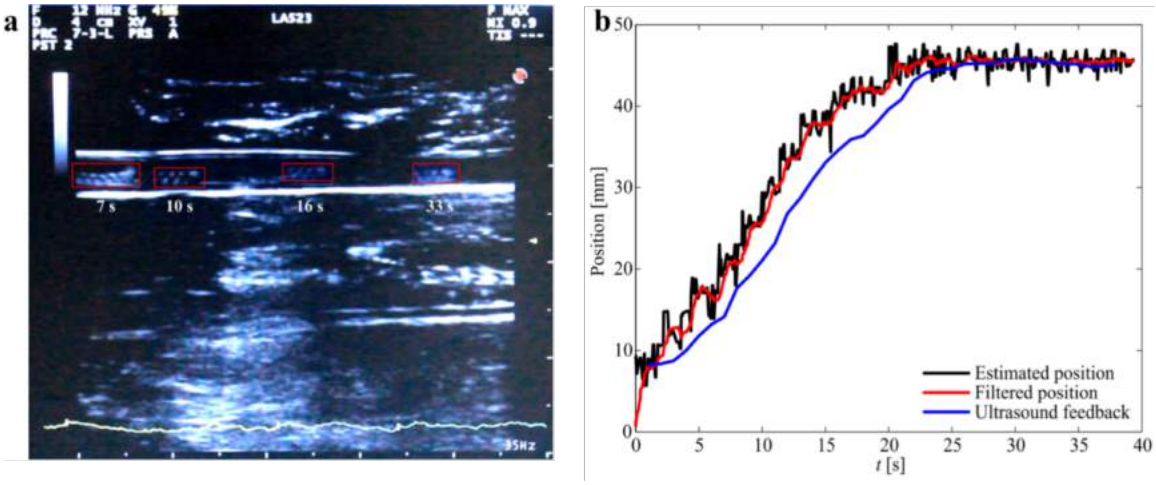

Fig. 2.9. Magnetic localization of a helical robot is achieved and compared to ultrasound feedback. (a) The helical robot is allowed to swim in whole blood and its position is detected using an ultrasound transducer (LA523 linear array ultrasound transducer, Esaote, Italy). The red rectangles indicate the position of the helical robot at different time instants. (b) The mean absolute position error between the magnetic tracking and ultrasound feedback is 2.6 mm.

reservoir is fixed above the magnetic field sensor array. Position of the helical robot is localized simultaneously using ultrasound feedback and magnetic tracking.

Fig. 2.9(a) shows the motion of the helical robot using ultrasound feedback for a depth of 5 cm. The frequency of the ultrasound waves is set to 12 MHz and the ultrasound system is adjusted to motion mode (M-mode) to acquire scans during propulsion. The thermal index score, mechanical index, and gain are 0.1, 0.9, and 49%, respectively.

Position of the helical robot is tracked from the acquired ultrasound scans and compared to the estimated position of the magnetic localization, as shown in Fig. 2.9(b). The mean absolute position error between the ultrasound and magnetic localization is 2.6 mm. This error is approximately equal to the error between the measured position using visual feedback and magnetic tracking. Again, this error can be caused by the field modeling errors and/or the sensors background noise.

3. MAGNETIC TRACKING FOR MAGNETIC RENDERING APPLICATIONS

In this chapter tracking of a magnetic dipole used to allow a user to feel magnetic force exerted from an electromagnetic-based haptic device will be discussed. The magnetic dipole is localized using two identical arrays of magnetic field sensors [48].

3.1 System Description

The system consists of an electromagnetic-based haptic device [41], two identical arrays of magnetic field sensors, a permanent magnet fixed on a wearable orthopedic finger splint and a validation board, as shown in Fig. 3.1. The electromagnetic-based haptic device used for magnetic rendering of volumetric shapes consists of an array of 9 electromagnetic coils. Each electromagnetic coil has inner and outer diameters of 24 mm and 38 mm, respectively. The height of the coil and the length of its low carbon steel core are 100 mm and 110 mm, respectively. The number of turns is 1429. Each of the electromagnetic coils is independently supplied with current using electric drivers (MD10C, Cytron Technologies Sdn. Bhd, Kuala Lumpur, Malaysia) and controlled via a MyRio control board (MyRio, National Instruments, Mopac, Expwy Austin, U.S.A). The electromagnetic coils are fixed to upper and lower plastic frames in order to keep all magnetization axes parallel to each other. The electromagnetic configuration of this haptic device provides a planar footprint of 150 mm$\times$150 mm and hight of 60 mm. The electromagnetic coils are used to generate magnetic forces on a Neodymium permanent magnet (S-10-05-N, N52, nickel-plated, supermanete, Gottmadingen, Germany). The permanent magnet has axial magnetization of 1.1579×10^{6} A.m^{-1} with thickness and diameter of 10 mm, 10 mm respectively. This magnet is attached to the tip of a wearable orthopedic finger splint,

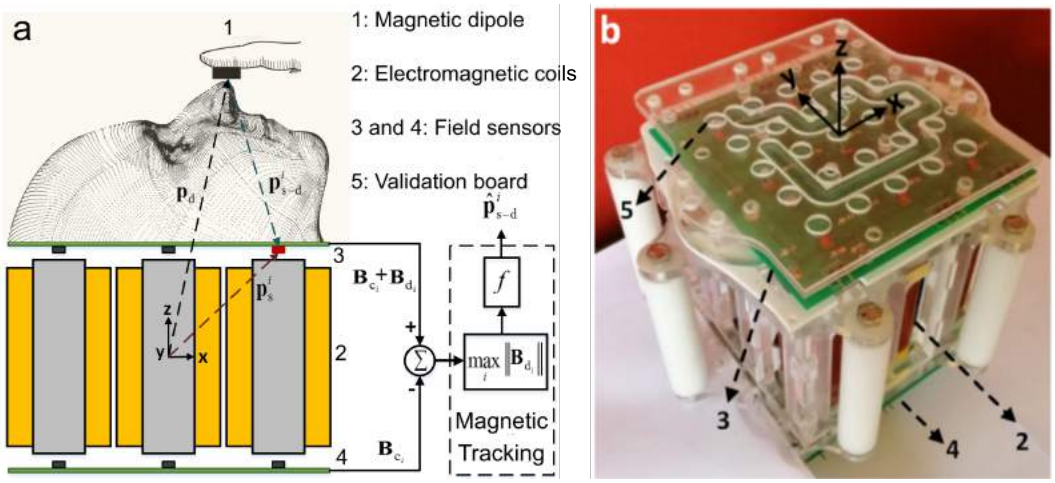

Fig. 3.1. Localization of a permanent magnet fixed on a finger splint is achieved using two identical layers of magnetic field sensors arrays in order to provide accurate position feedback for an electromagnetic-based haptic device. (a) A schematic representation of a magnetic dipole (1) at a position $\mathbf{p}_d$ during the interaction with the electromagnetic-based haptic device (2). The first array (3) is located on the upper side (the haptic interface side) and the second (4) on the lower side. The first array provides the generated field measurements from the wearable permanent magnet $\mathbf{B}_d$ and the electromagnetic coils $\mathbf{B}_c$. The second array provides the measurements from the electromagnetic-based haptic device only (background magnetic field). The subtraction between these arrays provides the field readings of the wearable permanent magnet. (b) The integration of the magnetic tracking system for magnetic rendering applications.

and enables the user to perceive the magnetic force from the system. Two arrays of magnetic field sensors (3D magnetic sensor TLV493DA1B6,Infineon Technologies AG,Munich,Germany) are fixed below and above the electromagnetic coils. The upper layer of magnetic field sensors is used to sense the magnetic field from the permanent magnet and the electromagnetic coils. The lower layer of magnetic field sensors is used sense the magnetic field from the electromagnetic coils. Both upper and lower layers are fixed away from the electromagnetic coils with the same distance so that the resulting signal form the subtraction of the two layers includes only the magnetic field from the permanent magnet. The application circuits of the magnetic field

sensors are designed in order to place two sensors in the center of the corresponding electromagnetic coil, one sensor is above the coil and the other is below it. Therefore a total of 18 magnetic field sensors are used.

3.2 Magnetic Tracking of the Permanent Magnet

The dipole used is a cylindrical permanent magnet with magnetic moment vector ($\mathbf{m}$) perpendicular to the finger of the user (Fig. 3.2). Magnetic force is applied using magnetic fields from electromagnetic coils ($\mathbf{B}_c$).

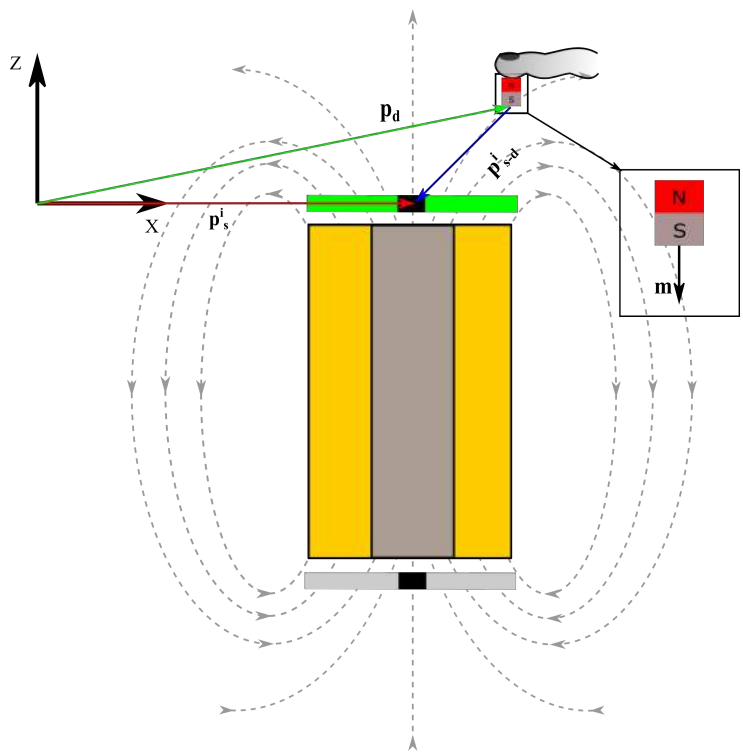

Fig. 3.2. Dipole model of the permanent magnet (shown magnified) and the magnetic field sensors are used to localize the permanent magnet. The permanent magnet (with magnetization $\mathbf{m}$) is moved by the user in the workspace of the haptic device. $\mathbf{p}^i_s$ is position vector to the ith sensor from a reference frame and $\mathbf{p}^i_{s-d}$ is position vector to the ith sensor from the permanent magnets frame of reference.

Let $\mathbf{p}_d$ be the position of the magnetic dipole, and two arrays of magnetic field sensors are fixed above and below the electromagnetic coils at the same distance with respect to the coils (Fig. 3.1(a)). Therefore, the ith magnetic field sensor mounted on the upper layer is subject to the following magnetic fields:

$$\mathbf{B}^i_{su} = \mathbf{B}_{di} + \mathbf{B}_{ci}, \tag{3.1}$$

where $\mathbf{B}^i_{su}$ is the magnetic field measured by the ith sensor due to the permanent magnet ($\mathbf{B}_{di}$) and the electromagnetic coils ($\mathbf{B}_{ci}$). The magnetic field generated by the coils ($\mathbf{B}_{ci}$) is determined directly by the corresponding ith sensor mounted on the lower array as a result of the magnetic symmetry of the coils. Therefore, the magnetic field affecting the ith sensor on the lower array is given by

$$\mathbf{B}^i_{sl} = \mathbf{B}_{ci}, \tag{3.2}$$

where $\mathbf{B}^i_{sl}$ is the magnetic field measured by ith sensor mounted on the lower layer of magnetic field sensors due to the electromagnetic coils. Fig. 3.3 shows a representative simulation result of the magnetic field generated by the electromagnetic coils and the wearable magnetic dipole. The coils are supplied with 1 A current. The magnetic dipole is located at the center of the coils at height of 30 mm. In order to estimate the position of the magnetic dipole ($\mathbf{p}_d$), first, the magnetic field measurement of the nearest ith sensor is selected, which is given by

$$\mathbf{B}_d = \max_i \|\mathbf{B}_{di}\|. \tag{3.3}$$

Second, the position of the magnetic dipole with respect to the ith sensor ($\mathbf{p}^i_{s-d}$) is estimated by a function f that maps the input fields ($\mathbf{B}_d$) to the position. A feed forward neural network algorithm is used to approximate the relation between field readings and the position (f) in real-time without iterations [49]. The neural network is trained on 1300 points in a workspace of $50 \times 50 \times 50$ around the magnetic dipole using back-propagation learning algorithm, based on Levenberg Marquardt technique.

Each data point contains the 3D field data ($\mathbf{B}_m$) for a given position $\mathbf{p}$ along x-, y and z-axis. These field points are calculated by

$$\mathbf{B}_m = -\mu_0 \nabla \phi(\mathbf{p}), \tag{3.4}$$

where μ_0 is the magnetic permeability of free space and $\phi(\mathbf{p})$ is the magnetic scalar potential. The neural network used consists of an input layer, output layer and five hidden layers, each contains 10 neurons. The mentioned neural network is implemented using MATLAB Neural Net Fitting Toolbox.

Third, the position of the magnetic dipole from a fixed frame of reference ($\mathbf{p}_d$) is determined using

$$\mathbf{p}_d = \mathbf{p}_s^i - \mathbf{p}_{s-d}^i, \tag{3.5}$$

where $\mathbf{p}_s^i$ is a fixed position vector to the ith sensor from the fixed frame of reference. The position of the magnetic dipole is then used to validate the magnetic tracking system under different cases of magnetic fields generated by the haptic interface.

3.3 Experimental Results of the Tracking System for Magnetic Rendering Applications

In order to validate the accuracy of the tracking system, a set of experiments are made while magnetic tracking is implemented that will be discussed. In each experiment a machined acrylic board is fixed 8.7 mm above the upper magnetic field sensors array. The validation board consists of 25 holes and a predefined path for the permanent magnet in a known fixed position from a reference point which is the center of the upper layer of magnetic field sensors.

3.3.1 Validation of the Tracking System Without Background Magnetic Field

To examine the magnetic tracking system in the absence of background magnetic field, the permanent magnet is localized using the validation board (Fig 3.3(a)) while

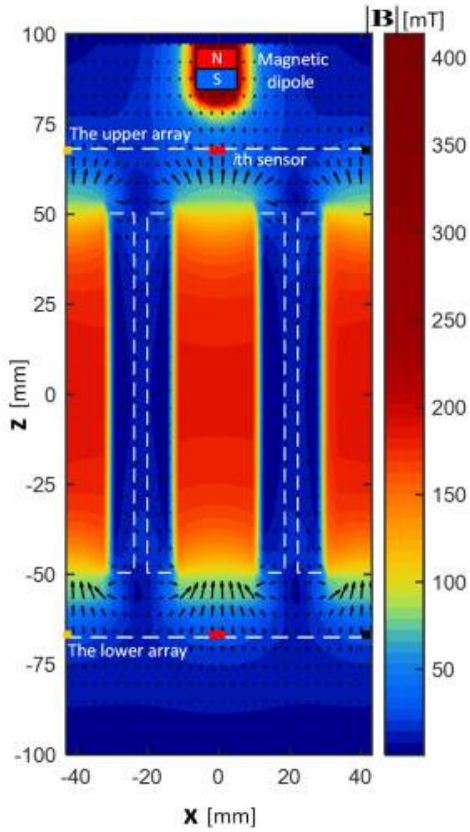

Fig. 3.3. Representative simulation result of the magnetic field generated by the electromagnetic coils for constant currents of 1 A. The magnetic dipole is located in the center of the coils at height of 30 mm.

the electromagnetic coils are not supplied with current. The maximum measured magnetic field from the upper array of magnetic field sensors is fed to the neural network to calculate $\mathbf{p}^i_{s-d}$, and then estimate $\mathbf{p}_d$ using (3.5). The estimated position of the permanent magnet is then compared to the position of the holes and the predefined path, as shown in Figs. 3.6-3.8. Figs. 3.3-3.5 show a representative experiment for magnetic tracking of the permanent magnet located in a known fixed position (0,0,8.7) with respect to a frame of reference. The absolute position error between the estimated and actual positions in this representative experiment is 0.345 mm.

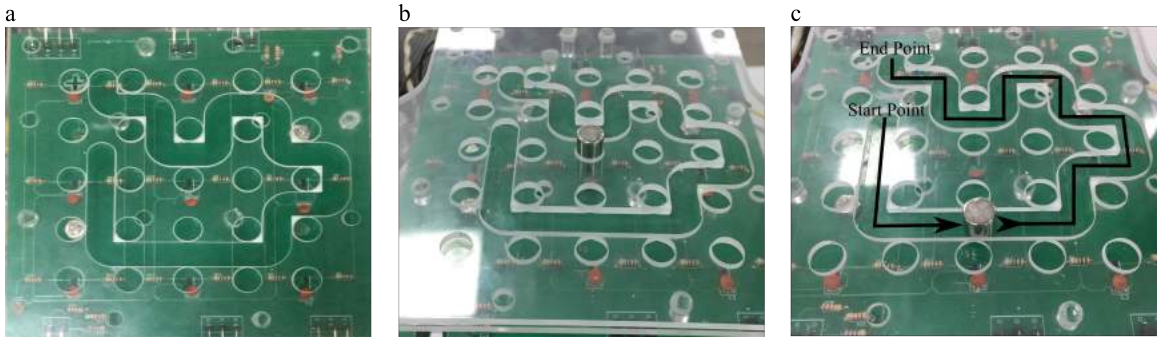

Fig. 3.4. Localization of a permanent magnet is achieved using 3D magnetic field sensors. (a) Machined acrylic board for the validation of magnetic tracking of the permanent magnet. (b) Permanent magnet is placed in the middle of the acrylic board at (0, 0, 8.7) mm in x-, y- and z-axis respectively. The position of the permanent magnet is estimated at this point using magnetic tracking. (c) The permanent magnet is moved in a predefined path with illustrated start and end points. The position of the permanent magnet is estimated along the path using magnetic tracking.

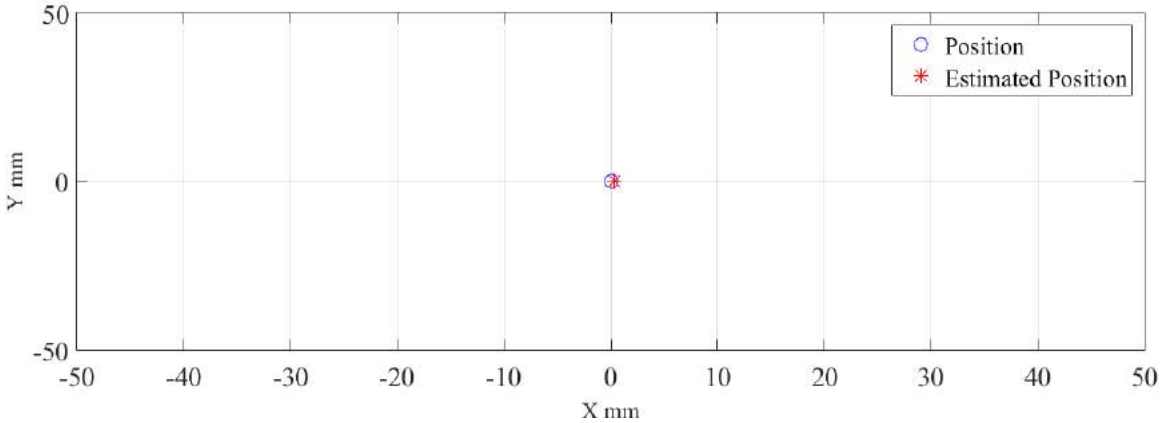

Fig. 3.5. Estimated position of the permanent magnet is compared to the actual position in x- and y-axis. The mean absolute error between the estimated and actual positions is 0.345 mm.

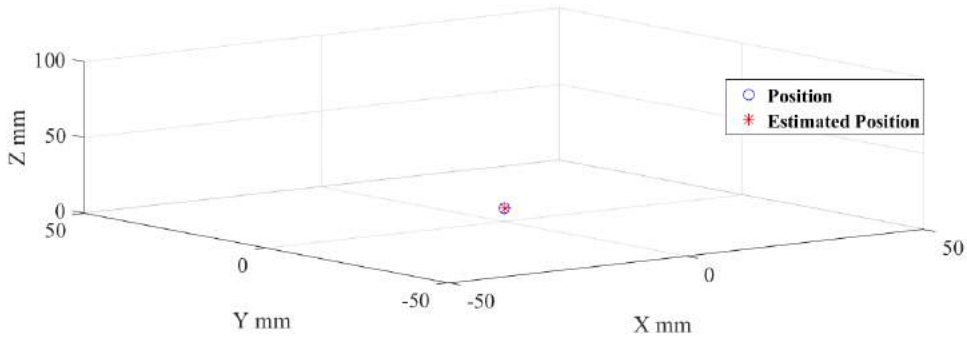

Fig. 3.6. Estimated position of the permanent magnet is compared to the actual position in x-, y- and z-axis.

This experiment is repeated 5 times for each hole and 6 times for the predefined path and the mean absolute position error is calculated as 0.806 ± 0.3 mm. This position error is due to SNR and the error from the neural network. The SNR is inversely proportional with the distance between the permanent magnet and the magnetic field sensors.

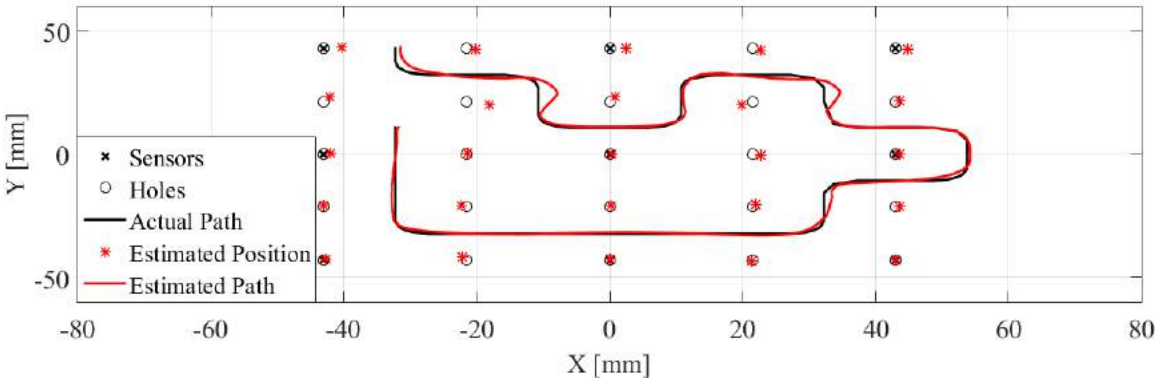

Fig. 3.7. Estimated position of the permanent magnet in 25 points and a predefined path is compared to the actual position in x- and y-axis. The mean absolute error between the estimated and actual positions is 0.806 ± 0.3 mm.

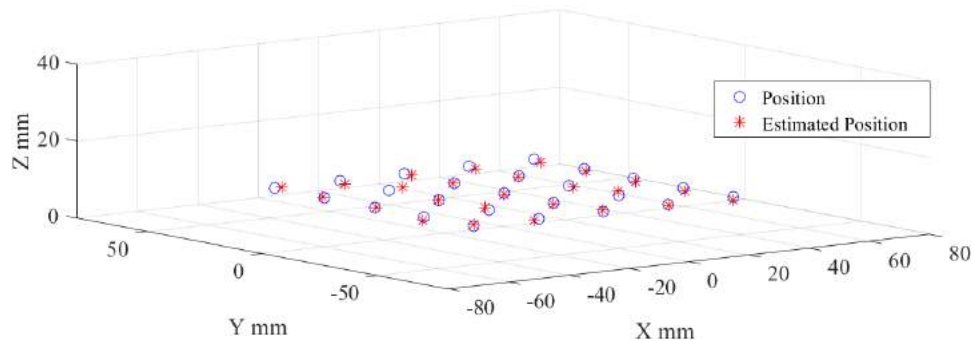

Fig. 3.8. Estimated position of the permanent magnet in 25 points is compared to the actual position in x-, y- and z-axis.

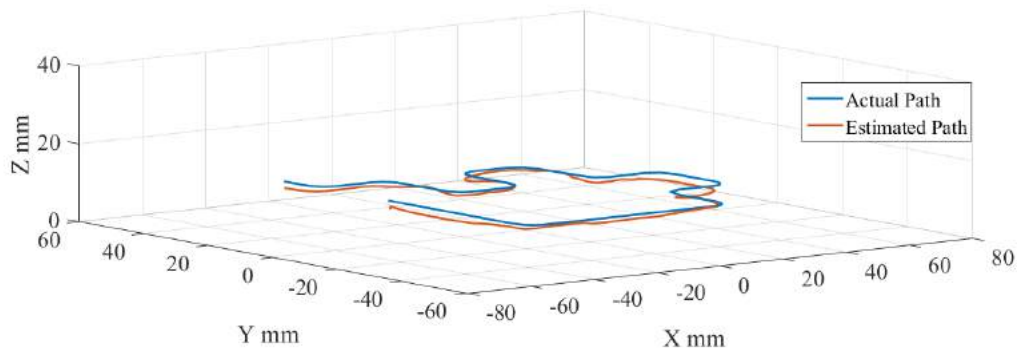

Fig. 3.9. Actual path of the permanent magnet is compared to the estimated path from the magnetic tracking through the predefined path in x-, y- and z-axis.

3.3.2 Validation of the Tracking System in The Presence of Constant Background Magnetic Field

In order to ensure that the tracking system can localize the permanent magnet properly while the electromagnetic coils are affecting the magnetic field sensors with background magnetic field, the same machined acrylic board mentioned before is used to validate the tracking accuracy while supplying the array of electromagnetic coils with 1 A current each. The lower magnetic field sensors array is used to measure the

background magnetic field from the coils to get $\mathbf{B}_c$ in equation (3.1) and then calculate $\mathbf{B}_d$ to estimate the position of the permanent magnet. The estimated position of the permanent magnet is then compared to the actual position from the reference point, as shown in Figs. 3.9-3.11. The mean absolute position error is calculated as 1.266 ± 0.431. This error is due to SNR and the fixation error between the validation board and the magnetic field sensors board and the fixation error between the upper and lower arrays of magnetic field sensors and the coils.

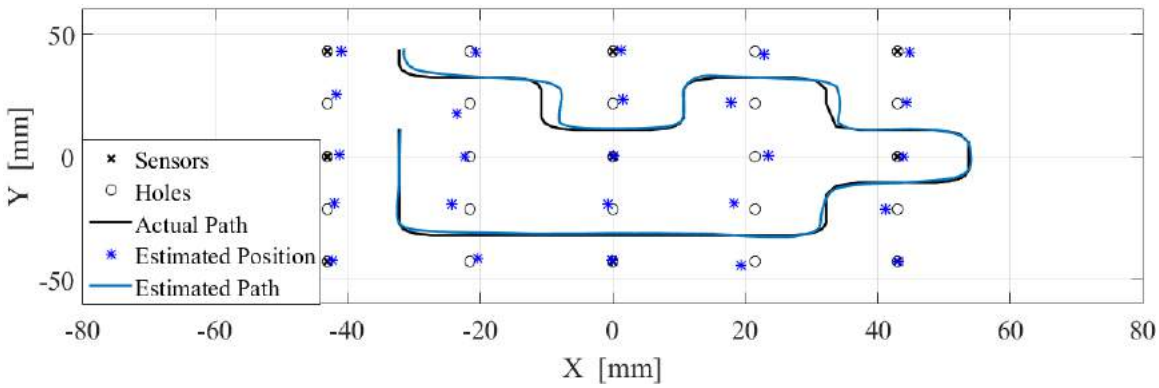

Fig. 3.10. Estimated position of the permanent magnet in 25 points and a predefined path is compared to the actual position in x- and y-axis while supplying the array of electromagnetic coils with 1 A current.

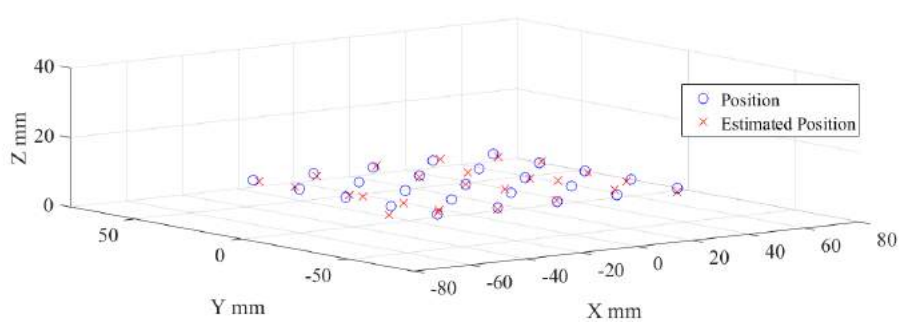

Fig. 3.11. Estimated position of the permanent magnet in 25 points is compared to the actual position in x-, y- and z-axis while supplying the array of electromagnetic coils with 1 A current. The mean absolute error is 1.266 ± 0.431.

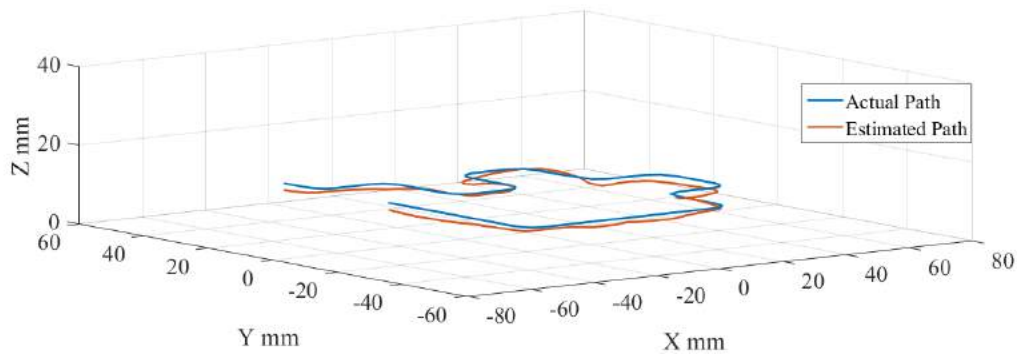

Fig. 3.12. Actual path of the permanent magnet is compared to the estimated position from the magnetic tracking through the predefined path in x-, y- and z-axis while supplying the array of electromagnetic coils with 1 A current.

3.3.3 Validation of the Tracking System in The Presence of Variable Background Magnetic Field

The magnetic rendering process can require sudden changes in the magnetic field from the electromagnetic coils. Therefore, it is important to ensure that the tracking system can perform accurately under this condition. Two experiments are made in order to ensure proper localization under variable background magnetic field. First, the electromagnetic coils are supplied with periodic variable current that varies from 0 A to 1 A with 0.3 Hz frequency satisfying the following equation

$$I = \frac{1}{2}\sin x + 0.5, \tag{3.6}$$

where I is the supplied current to the electromagnetic coils, x is incremented from 0 to 2π iteratively with steps of 0.1. Fig. 3.12 shows the readings of a magnetic field sensor affected by the periodic variable magnetic field from the electromagnetic coils in the z-direction.

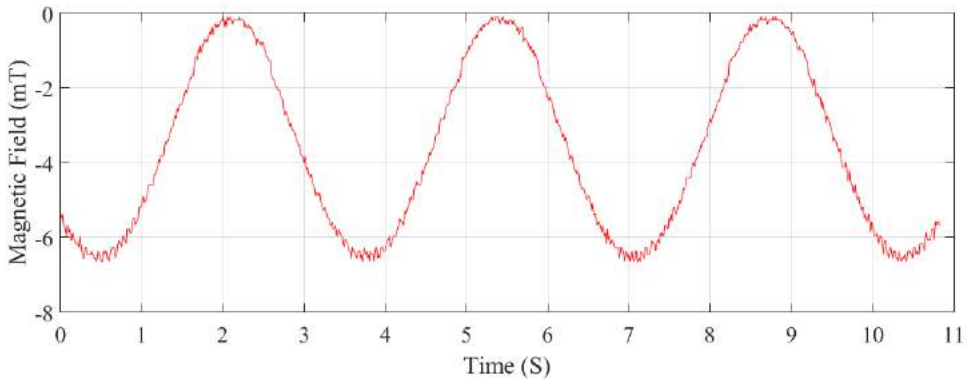

Fig. 3.13. Magnetic field sensor readings in the z-direction while it is affected by the periodic variable magnetic field from the electromagnetic coils.

The permanent magnet is then localized using the magnetic tracking system. The validation of the tracking accuracy is made using the machined acrylic board to test the performance of the system. The mean absolute position error between the actual and the estimated positions (Figs. 3.13-3.15) of the permanent magnet is 0.912 $\pm$ 0.332 mm.

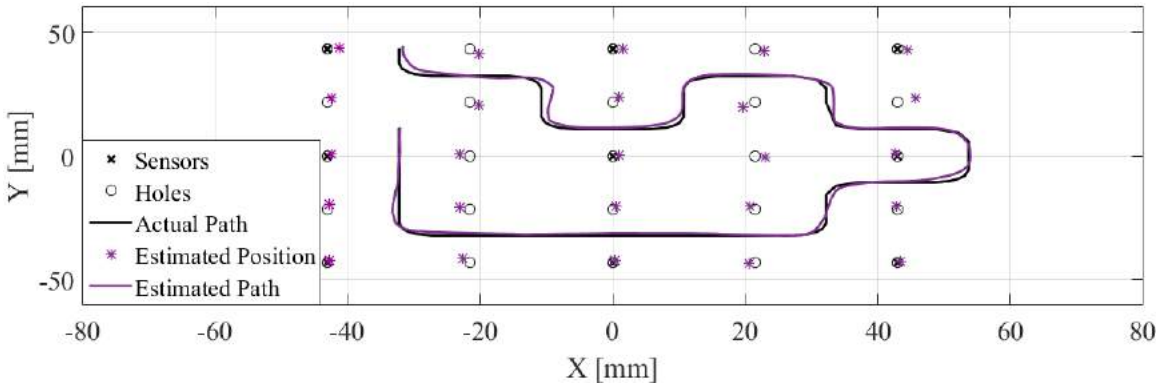

Fig. 3.14. Estimated position of the permanent magnet in 25 points an a predefined path is compared to the actual position in x- and y-axis while supplying the array of electromagnetic coils with periodic variable current.

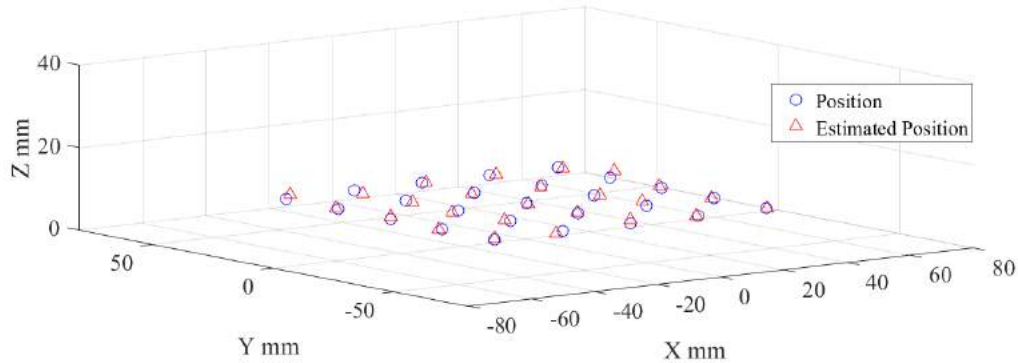

Fig. 3.15. Estimated position of the permanent magnet in 25 points is compared to the actual position in x-, y- and z-axis while supplying the array of electromagnetic coils with periodic variable current. The mean absolute error between the estimated position and the actual position is 0.912 ± 0.332 mm.

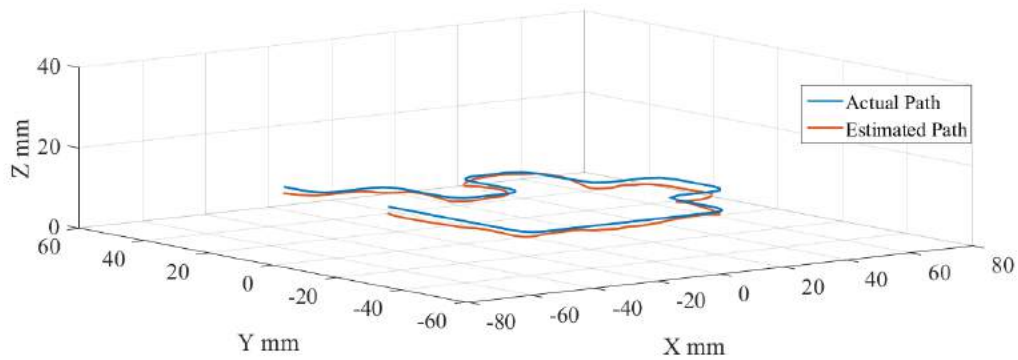

Fig. 3.16. Actual path of the permanent magnet is compared to the estimated position from the magnetic tracking through the predefined path in x-, y- and z-axis while supplying the array of electromagnetic coils with periodic variable current.

Second, the electromagnetic coils are supplied with variable current from 0 to 1 A, the value of the supplied current is chosen randomly within the mentioned limits. Fig. 3.16 shows the readings of a magnetic field sensor affected by the random variable magnetic field from the electromagnetic coils in the z-direction.

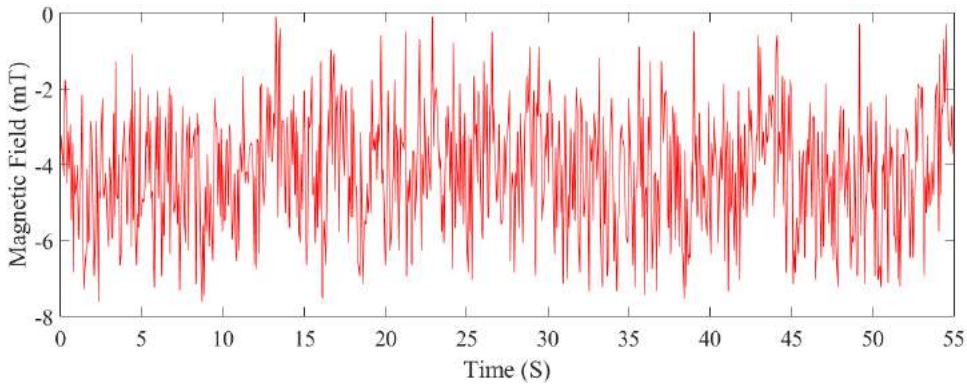

Fig. 3.17. Magnetic field sensor readings in the z-direction while it is affected by random variable magnetic field from the electromagnetic coils.

The permanent magnet is then localized using the magnetic tracking system. The validation of the tracking accuracy is made using the machined acrylic board to test the performance of the system. The mean absolute position error between the estimated position and the actual position (Figs. 3.17-3.19) of the permanent magnet in this case is 0.864 ± 334 mm.

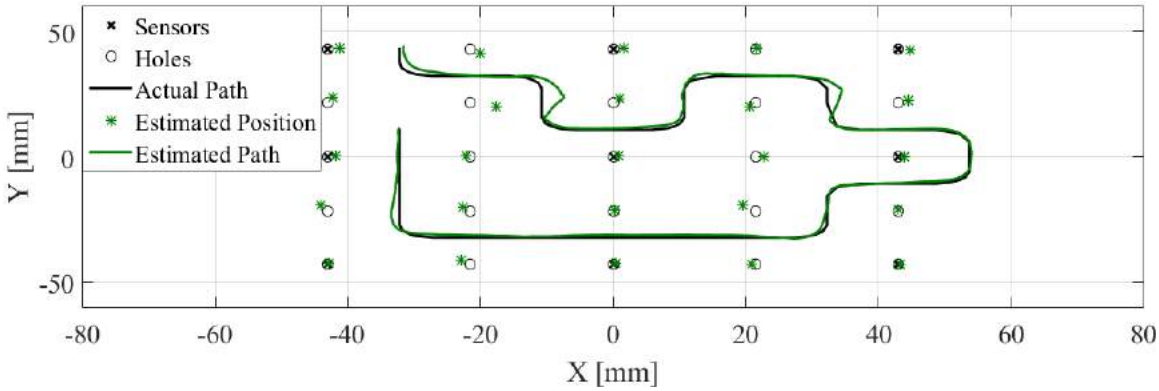

Fig. 3.18. Estimated position of the permanent magnet in 25 points and a predefined path is compared to the actual position in x- and y-axis while supplying the array of electromagnetic coils with random variable current.

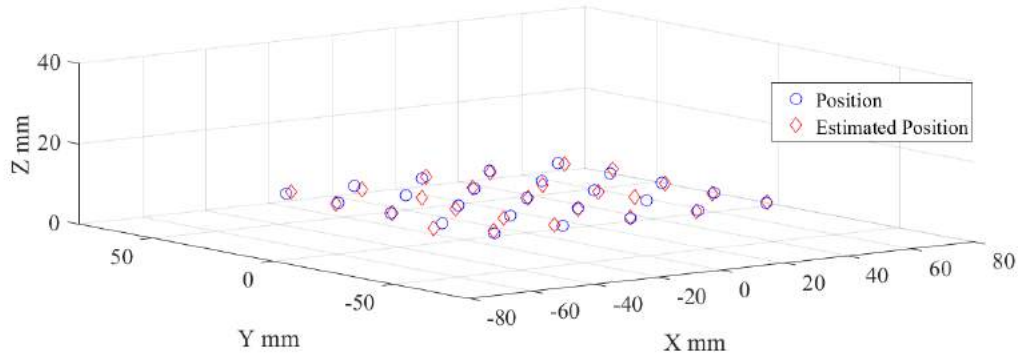

Fig. 3.19. Estimated position of the permanent magnet in 25 points is compared to the actual position in x-, y- and z-axis while supplying the array of electromagnetic coils with random variable current that varies from 0-1A. The mean absolute error between the estimated position and the actual position is 0.864 ± 0.334 mm.

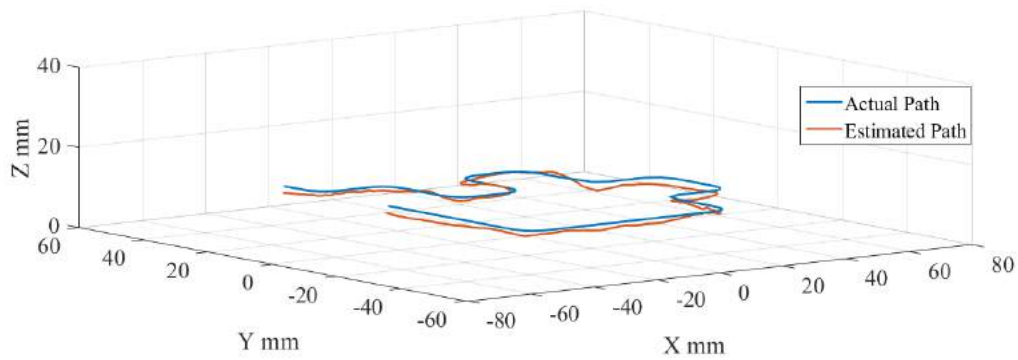

Fig. 3.20. Actual path of the permanent magnet is compared to the estimated position from the magnetic tracking through the predefined path in x-, y- and z-axis while supplying the array of electromagnetic coils with random variable current that varies from 0-1 A.

3.3.4 Benefits of Using an Extra Layer of Magnetic Field Sensors Rather Than Modeling The Background Magnetic Field

As mentioned before, in (3.1) the term ($\mathbf{B}_c$) is generated due to the superposition of an array of 9 electromagnetic coils (3×3). The magnetic field generated by a single electromagnetic coil at the ith sensor is a result of the contribution of the coil ($\mathbf{B}_{coil}$) and the ferromagnetic core ($\mathbf{B}_{core}$). The generated magnetic field by the coil can be represented by

$$\mathbf{B}_{coil}(\mathbf{p}) = \nabla \times \mathbf{A}(\mathbf{p}), \tag{3.7}$$

where $\mathbf{A}(\mathbf{p})$ is the magnetic vector potential. The generated magnetic field by the ferromagnetic core can be represented by

$$\mathbf{B}_{core}(\mathbf{p}) = -\mu_0 \nabla \phi(\mathbf{p}), \tag{3.8}$$

where μ_0 is the magnetic permeability of free space and $\phi(\mathbf{p})$ is the magnetic scalar potential. $\mathbf{A}(\mathbf{p})$ and $\phi(\mathbf{p})$ are calculated using the multipole expansion method. Therefore, $\mathbf{B}_c$ can be estimated using (3.7) and (3.8). (3.1) can now be represented as:

$$\mathbf{B}^i_{su} = \mathbf{B}_d + \widehat{\mathbf{B}}_c, \tag{3.9}$$

where $\widehat{\mathbf{B}}_c$ is the estimated field of the electromagnetic coils at the ith sensor mounted on the upper layer. Petruska *et* al. have investigated the bounds of error in the multipole expansion [50]. It was demonstrated that the first nine components of the multipole expansion are quite accurate (error $< 2\%$) for distances greater than 1.5 the minimum bounding sphere radius of the electromagnetic coil (Fig. 3.20), which can be calculated by

$$R_s = \left(\frac{V}{2\pi}\right)^{\frac{1}{3}} \frac{\sqrt{\beta^2+1}}{\beta^{\frac{2}{3}}}, \tag{3.10}$$

where R_s is the radius of the minimum bounding sphere that encloses the electromagnetic coil, V is the volume of the electromagnetic coil and β is the diameter-to-length aspect ratio. In our case the radius of the minimum bounding sphere is 58.19 mm, which means that for obtaining accurate estimation of the magnetic field generated

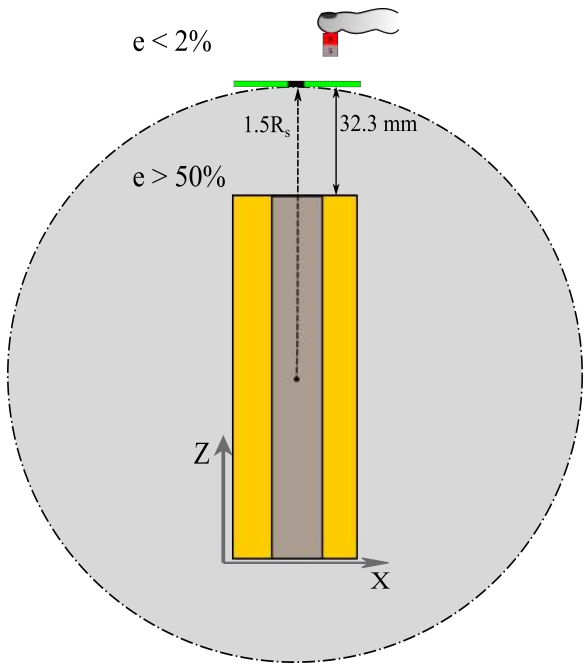

Fig. 3.21. The bounds of error of the estimated magnetic field using the multipole expansion method.

by the electromagnetic coils, the sensors have to be mounted at least 32.29 mm above the surface of the coils. However, due to the limited projection of the magnetic force in the electromagnetic based haptic interface, it is not practical to lose this axial distance. One solution is mounting the magnetic field sensors outside the workspace of the haptic interface as the magnetic field generated by the tracked permanent magnet at the farthest point of the workspace is 0.6 mT, which is higher than the resolution and noise of the sensor. However, mounting the sensors outside the workspace would prevent the integration of augmented visualization as the sensors board will obstruct the line of sight between the user and the rendered shape as show in Fig. 3.21.

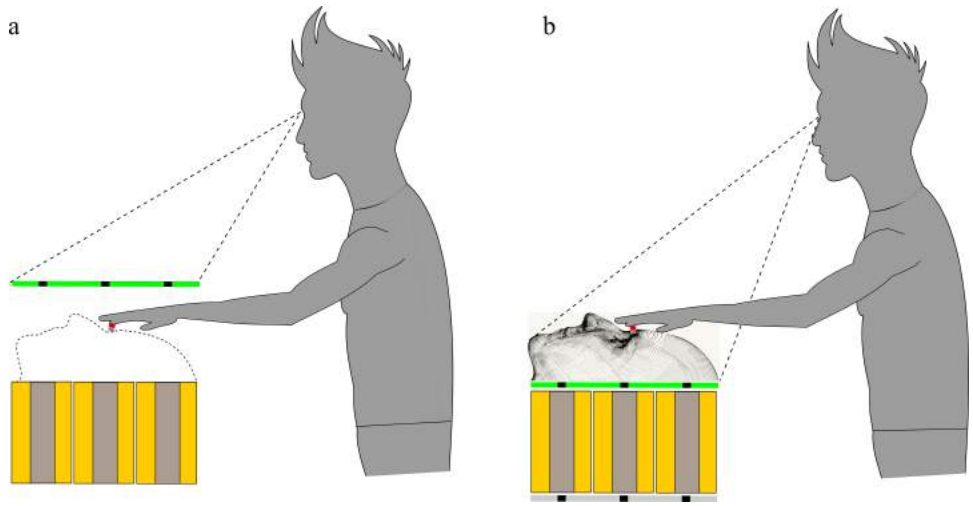

Fig. 3.22. Mounting the magnetic field sensors outside the workspace of the electromagnetic based haptic interface prevents the integration of augmented visualization for the rendered object. (a) Line of sight of the user is obstructed by the magnetic field sensors board. (b) The user can visualize the rendered object after integrating augmented visualization.

Finally, The integration of an extra layer of magnetic field sensors to exploit the magnetic symmetry of the haptic system allows avoiding the error in modeling the background magnetic field generated from the electromagnetic coils; which is a result of the contribution of the coils, the ferromagnetic cores and mutual inductance between coils, and enhances the compactness of the system to increase the capability of integrating augmented visualization. The subtraction between the measurements of the magnetic field sensors decreases any current noise of significance in the range of the sensor noise, that is symmetrically represented across the coil poles.

4. CONCLUSIONS

In this work, magnetic tracking technique is implemented in two applications. The first application is the tracking of a helical microrobot for clearing superficial blood clots. The tracking accuracy is characterized using visual feedback with position tracking error of 2.5 ± 0.4 mm. Closed loop motion control is achieved based on the estimated position of the robot towards blood clots *in vitro* with average steady state error of 0.74 ± 1.9 mm. Tracking of the helical microrobot is also implemented inside a rabbit aorta and a catheter segment filled with whole blood and the results was validated using ultrasound feedback. The mean absolute position error between ultrasound and magnetic tracking is 2.6 mm. The tracking and control of the helical robot allows removal of blood clots at an average removal rate of 0.67 ± 0.47 mm^3/min. The second application is the tracking of a permanent magnet fixed on an orthopedic finger splint used in magnetic rendering applications. The tracking accuracy is validated at different conditions using a machined acrylic board with 25 holes for the permanent magnet with known positions and a predefined path. The first validating condition is tracking of the permanent magnet without background magnetic field used in magnetic rendering and the position tracking mean absolute error is 0.806 ± 0.3 mm. The second condition is tracking of the permanent magnet under constant background field with mean absolute position tracking error of 1.266 ± 0.431 mm. The third condition is tracking of the permanent magnet under periodic variable background field with mean absolute position tracking error of 0.912 ± 0.332 mm. The fourth condition is tracking of the permanent magnet under random variable magnetic field with mean absolute position tracking error of 0.864 ± 0.334 mm. Finally, the benefits of using the extra layer of magnetic field sensors to eliminate the background magnetic field generated from the electromagnetic coils rather than modeling the background field is discussed.

5. FUTURE WORK

As a future work for this study, helical robots will be tracked at a relatively larger distance from the magnetic field sensors which will be helpful for clearing blood clots in deep veins. This can be achieved using magnetic field sensors with higher sensitivity. It is essential to implement a planar array of sensors to enhance the tracking of the helical robot during propulsion inside real blood vessels with bifurcations, as the implemented linear array is difficult to align with blood vessels in real *in vivo* applications. Regarding the magnetic tracking of the permanent magnet used in the magnetic rendering process, the tracking system can contribute in stiffness rendering of objects which can be used in many medical applications as it can help to render affected organs, for example, liver fibroses can be detected from the stiffness of the liver as it makes the liver stiffer than its normal state. Magnetic tracking for multiple dipoles can also be implemented in order to track all the fingers of the user.

APPENDIX

A. MAGNETIC TRACKING SYSTEMS

As discussed before, two systems have been developed. The first system is for tracking of a microrobot while performing medical tasks. The second system is for tracking of a dipole used in magnetic rendering applications. In order to build the mentioned two systems, an array of magnetic field sensors (Fig. A.1) is used. The distribution of the sensors is different in the two systems as the application is different. NI myRIO 1900 (MyRio, National Instruments, Mopac, Expwy Austin, U.S.A) is used as the controller for the tracking system and the programming of the system is made using NI LABVIEW.

Fig. A.1. 3D magnetic sensor TLV493D-A1B6 used in the magnetic tracking systems

A.1 Sensor Specifications

The magnetic field sensor provides accurate three-dimensional magnetic field sensing up to ± 130 mT with extremely low power conption (approximately 10μA) in a small 6-pin package. The sensitivity of sensor is 0.1 mT and the background noise of the sensor is 0.1 mT. With its magnetic field detection in x-, y- and z-directions (Fig. A.2) the sensor reliably measures three-dimensional, linear and rotation movements.

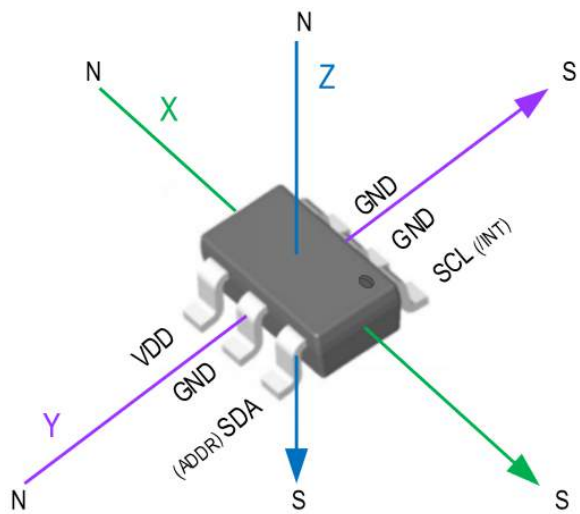

Fig. A.2. Sensing axes of the 3D magnetic field sensor

The digital output data is provided via 2-wire based I^2C interface with 12-bit data resolution for each measurement direction (x, y, z). The recommended data transfer rate of the magnetic field sensor using I^2C protocol is fast mode (400 Kbit/s), that means a communication reading of all data from the sensor requires a start condition for the I^2C protocol , 63 bits transfer and a stop condition for the I^2C protocol at 400 kbit/s, this means approximately 165 μs. After power up the sensor reads the voltage on the SDA (Serial Data) pin for 200 μs, if the voltage level is HIGH (digital '1') the sensor automatically specifies address (5E$_H$) for itself, and if the voltage level is LOW (digital '0') the sensor automatically specifies address (1F$_H$) for itself. This way it is possible to configure two sensors on the same I^2C bus. Additionally to the SDA

pin level to configure the sensor address, there are two bits (IICAddr) in the write register MOD1 of the sensor that allow to set an address. Therefore, combining the SDA pin levels with the two bits, up to eight sensors can be configured at start up on the same I^2C bus. Now each of the eight sensors has a specific address (summarized in the following table). The data transfer to any sensor will start when the master (myRIO 1900) addresses the desired sensor address.

Sesnor	SDA pin at power up	IICAddr bits	Address_{HEX}
0	HIGH	11	4A
1	HIGH	10	4E
2	HIGH	01	5A
3	HIGH	00	5E
4	LOW	11	B
5	LOW	10	1B
6	LOW	01	F
7	LOW	00	1F

Fig. A.3 shows the application circuit for the sensor connections. R_1 and R_2 are pull up resistors their values are 1.2 KΩ. The serial resistances R between SDA /SCL and Pull up resistors R_1/R_2 are used to avoid reflections on longer bus lines causing ground bouncing on sensor side and communication issues. The series resistance R between myRIO SCL pin and the pull up resistor R_2 together with the capacitance C_2 to ground provides additional EMC (Electromagnetic Compatibility) filtering, the value of C_2 is 200 pF. C_1 and C_{BUF} provide additional EMC filtering and their values are 100 nF.

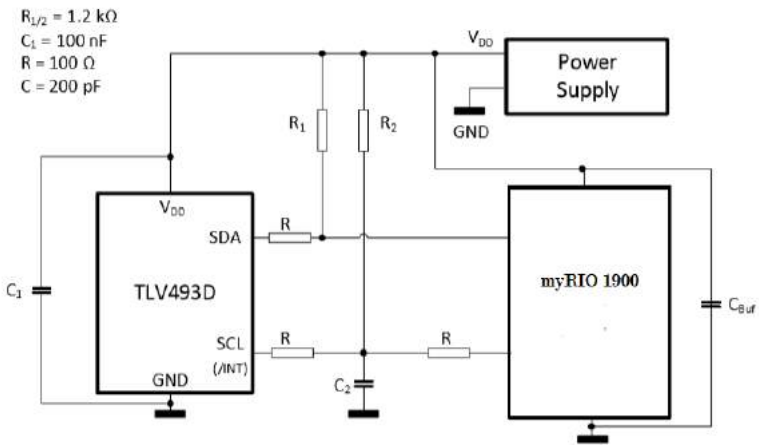

Fig. A.3. Application circuit for the magnetic field sensor and myRIO

Fig. A.4 shows the application circuit for 8 sensor connections. The power for the sensors should be supplied from digital output pins of myRIO (3.3 Volts) and can not be supplied from one power supply unit as the sensors have to be powered in sequence to ensure correct addressing.

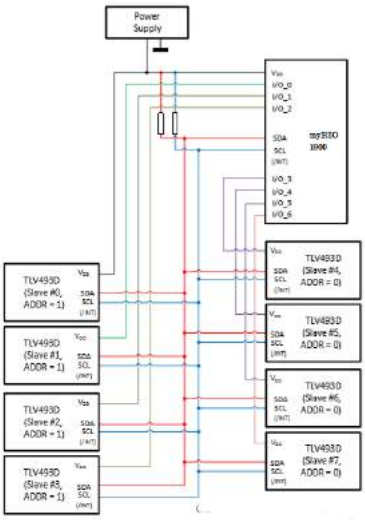

Fig. A.4. Application circuit for 8 magnetic field sensors and myRIO

A.2 Application Circuit for Magnetic Field Sensors for Tracking of Microrobots

For the microrobot tracking an array of 16 magnetic field sensors is used. MyRIO 1900 has two separate I^2C buses so it is possible to divide the 16 sensors on the two buses. The sensors are aligned linearly to track the microrobot motion in a linear path.

The design of the PCB used in magnetic tracking of microrobots is made using CadSoft Eagle software. Figs. A.5,A.6 show the implemented design of the application circuit and the PCB after manufacturing.

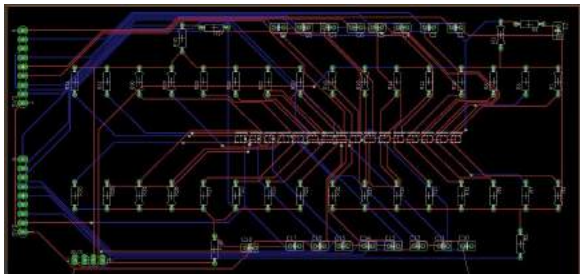

Fig. A.5. CadSoft Eagle PCB design for magnetic tracking of the microrobot.

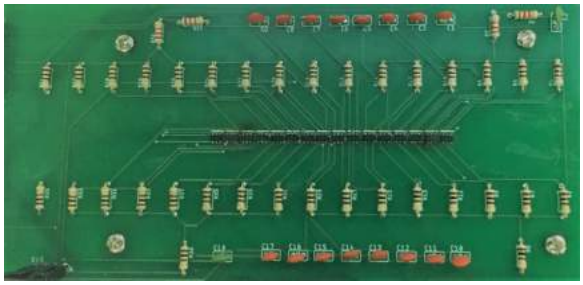

Fig. A.6. PCB for magnetic tracking of the microrobot after manufacturing.

A.3 Application Circuit for Magnetic Field Sensors used in Magnetic Rendering applications

For magnetic rendering, 2 typical arrays of magnetic field sensors are used. Each array consists of 9 magnetic field sensors. The circuits are designed in order to place two sensors in the center of the corresponding electromagnetic coil, one sensor is above the coil and the other is below it, as shown in Fig. A.7.

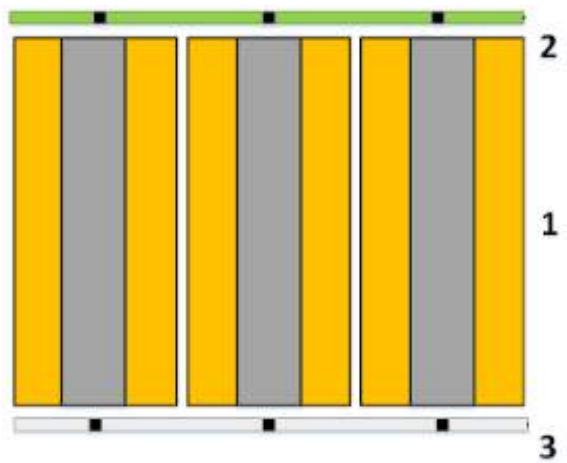

Fig. A.7. Sensors distribution with respect to the electromagnetic coils. (1) Electromagnetic coils used in magnetic rendering. (2) Upper sensors array, each sensor is in the center of an electromagnetic coil. (3) Lower sensors array.

As mentioned before, myRIO 1900 has two separate I^2C buses which can operate 16 magnetic field sensors according to the sensors specifications. In this system it is required to operate 18 magnetic field sensors. Therefore, two bidirectional analog multiplexers (8-Channel Analog Multiplexer/Demultiplexer, TOSHIBA, Tokyo, Japan) are used in order to route the SDA line and the SCL line from the I^2C bus to several outputs, as shown in Fig. A.8. The selection lines of the bidirectional multiplexers are supplied from myRIO 1900 digital output pins to select the routing of the I^2C bus.

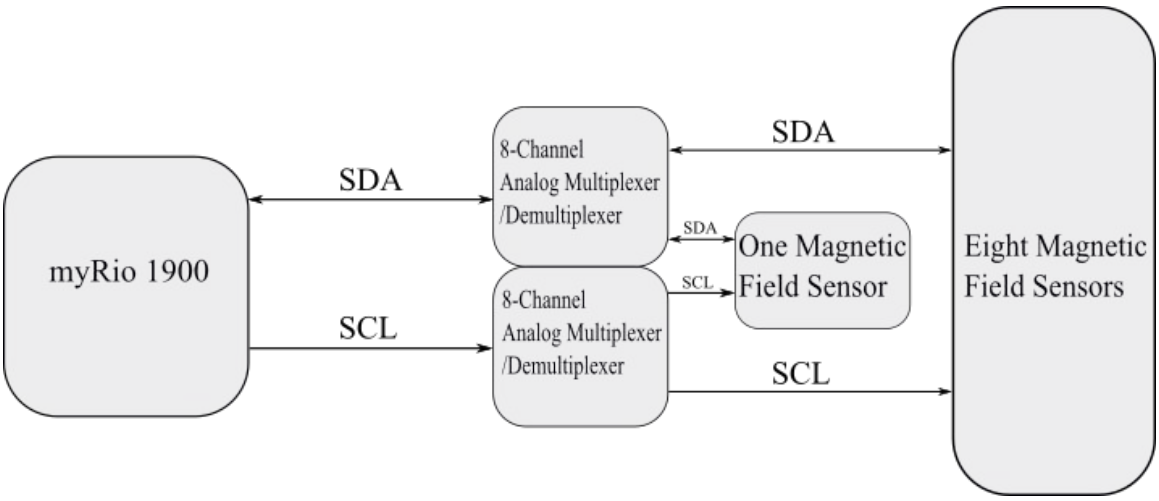

Fig. A.8. Two bidirectional multiplexers are connected to myRIO 1900 and the magnetic field sensors in order to route the I^2C bus signals to several arrays of sensors.

Bidirectional multiplexing of a signal is routing the signal into different outputs or selecting one of several input signals and forward the selected input into a single line. As I^2C communication protocol is a bidirectional protocol because the SDA line is used to send data bytes from master to slave and vice versa it is required to use a bidirectional multiplexer.

The design of the PCB used in magnetic tracking for magnetic rendering applications is made using CadSoft Eagle software. Figs. A.9,A.10 show the implemented design of the application circuit and the PCB after manufacturing. The upper and lower arrays are identical. Therefore, same design was used for both arrays.

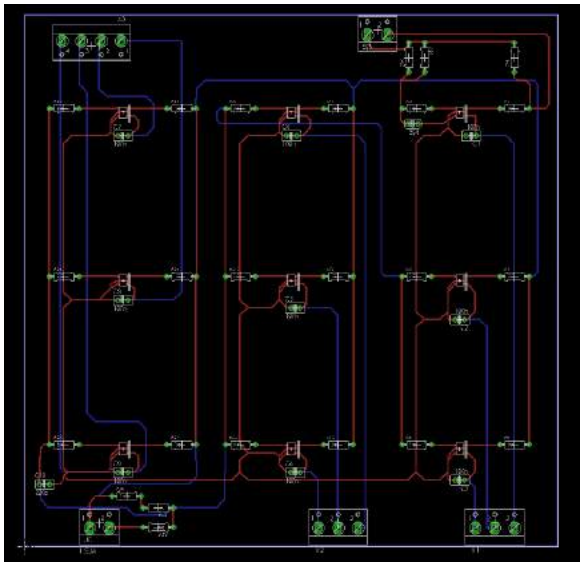

Fig. A.9. CadSoft Eagle PCB design used in the magnetic tracking system for magnetic rendering applications.

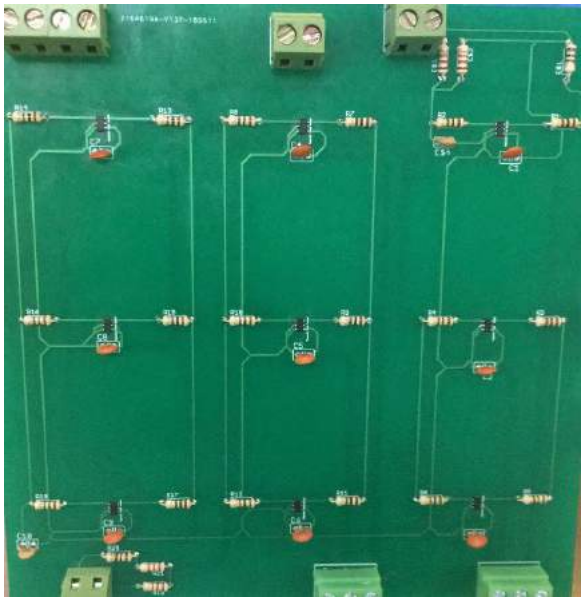

Fig. A.10. PCB for magnetic rendering after manufacturing.

LIST OF REFERENCES

LIST OF REFERENCES

[1] J. Mills, V. Tiwari, and S. Fairhurst, "Localization of binary mergers with gravitational wave detectors of second and third generation," *ArXiv e-prints*, August 2015.

[2] P. Bon, N. Bourg, S. Lecart, S. Monneret, E. Fort, and J. Leveque-Fort, "Three-dimensional nanometre localization of nano particles to enhance super-resolution microscopy," *Nature Communications*, vol. 6, pp. 7746–, July 2015.

[3] J. M. Buades, F. J. Perales, and J. Varona, "Real time segmentation and tracking of face and hands in vr applications," *3rd International Workshop on Articulated Motion and Deformable Objects*, vol. 3179, January 2004.

[4] B. J. Nelson, I. K. Kaliakatsos, , and J. J. Abbott, "Microrobots for minimally invasive medicine," *Annual Review of Biomedical Engineering*, vol. 12, no. 1, April 2010.

[5] Y. Ma, W. Jia, C. Li, J. Yang, Z.-H. Mao, and M. Sun, "Magnetic hand motion tracking system for human-machine interaction," *Electronics Letters*, vol. 46, no. 9, pp. 621–623, May 2010.

[6] I. S. M. Khalil, P. Ferreira, R. Eleutrio, C. L. de Korte, and S. Misra, "Magnetic-based closed-loop control of paramagnetic microparticles using ultrasound feedback," *in Proceedings of the IEEE International Conference on Robotics and Automation (ICRA)*, pp. 3807–3812, May-June 2014.

[7] M. Fluckiger and B. Nelson, "Ultrasound emitter localization in heterogeneous media," *Proc. IEEE Int. Conf. Eng. Med. Biol. Soc*, pp. 2867–70, August 2007.

[8] I. S. M. Khalil, D. Mahdy, A. E. Sharkawy, R. R. Moustafa, A. F. Tabak, M. Elwi, S. Hesham, N. Hamdi, A. Klingner, A. Mohamed, and M. Sitt, "Mechanical rubbing of blood clots using helical robots under ultrasound guidance," *IEEE Robotics and Automation Letters*, vol. 3, no. 2, pp. 1112–1119, April 2018.

[9] A. Filippeschi, N. Schmitz, M. Miezal, G. Bleser, E. Ruffaldi, and D. Stricker, "Survey of motion tracking methods based on inertial sensors: a focus on upper limb human motion," *Sensors*, vol. 17, no. 6, June 2017.

[10] Z. Liu, L. Zhang, Q. Liu, Y. Yin, L. Cheng, and R. Zimmermann, "Fusion of magnetic and visual sensors for indoor localization: Infrastructure-free and more effective," *IEEE TRANSACTIONS ON MULTIMEDIA*, vol. 19, no. 4, pp. 874–888, April 2017.

[11] J. Kelly and G. S. Sukhatme, "Visual-inertial sensor fusion: Localization, mapping and sensor-to-sensor self-calibration," *The International Journal of Robotics Research*, vol. 30, no. 1, pp. 57–79, November 2010.

[12] K. M. Popek, T. Hermans, , and J. J. Abbott, "First demonstration of simultaneous localization and propulsion of a magnetic capsule in a lumen using a single rotating magnet," *in Proceedings of the IEEE International Conference on Robotics and Automation (ICRA)*, pp. 1154–1160, May 2017.

[13] S. Yim and M. Sitti, "3-d localization method for a magnetically actuated soft capsule endoscope and its applications," *IEEE Transactions on Robotics*, vol. 29, no. 5, pp. 1139–1151, October 2013.

[14] D. Son, S. Yim, and M. Sitti, "A 5-d localization method for a magnetically manipulated untethered robot using a 2-d array of halleffect sensors," *IEEE/ASME Transactions on Mechatronics*, vol. 21, no. 2, pp. 708–716, April 2016.

[15] A. Plotkin, O. Shafrir, E. Paperno, and D. Kaplan, "Magnetic eye tracking: A new approach employing a planar transmitter," *IEEE transactions on biomedical engineering*, vol. 57, no. 5, pp. 1209–1215, March 2010.

[16] R. Iustin, J. Linder, E. Isberg, T. Gustafsson, and B. Lennernas, "A model based positioning system," *Patent. WO 2008/079071 A1, World Intellectual Property Organization*, 2008.

[17] J. M. Gilbert, S. I. Rybchenko, S. R. E. R Hofe, M. J. Fagan, R. K. Moore, and P. Green, "Isolated word recognition of silent speech using magnetic implants and sensors," *Medical engineering and physics*, vol. 32, no. 10, pp. 1189–97, December 2010.

[18] Y. Liu, Y. Wang, D. Yan, and Y. Zhou, "Dpsd algorithm for ac magnetic tracking system," *IEEE Symposium on Virtual Environments, Human-Computer Interfaces and Measurement Systems*, pp. 101–106, 2004.

[19] P. Berkelman, B. Tix, and H. Abdul-Ghani, "Electromagnetic position sensing and force feedback for a magnetic stylus with an interactive display," *IEEE MAGNETICS LETTERS*, vol. 10, pp. 1–5, 2019.

[20] T. L. Baldi, M. Mohammadi, S. Scheggi, and D. Prattichizzo, "Using inertial and magnetic sensors for hand tracking and rendering in wearable haptics," *In Proc. IEEE World Haptics Conference (WHC)*, pp. 381–387, 2015.

[21] I. S. M. Khalil, Y. Michel, B. Su, and S. Misra, "feeling paramagnetic microparticles trapped inside gas bubbles: a tele-manipulation study," *in Proceedings of the International Conference on Manipulation, Manufacturing and Measurement on the Nanoscale (3M Nano)*, pp. 225–230, July 2016.

[22] I. S. M. Khalil, A. F. Tabak, A. Hosney, A. Mohamed, A. Klingner, M. Ghoneima, and M. Sitti, "Sperm-shaped magnetic microrobots: fabrication using electrospinning, modeling, and characterization," *in Proceedings of the IEEE International Conference on Robotics and Automation (ICRA)*, pp. 1939–1944, may 2016.

[23] D. Mahdy, A. Mohamed, A. Klingner, A. Tammam, A. Wahdan, M. Serry, and I. S. M. Khalil, "Experimental characterization of helical propulsion in newtonian fluids and viscoelastic environments," *in Proceedings of the International Conference on Manipulation, Manufacturing and Measurement on the Nanoscale (3M Nano)*, pp. 319–322, August 2017.

[24] M. P. Kummer, J. J. Abbott, B. E. Kartochvil, R. Borer, A. Sengul, and B. J. Nelson, "Octomag: an electromagnetic system for 5-dof wireless micromanipulation," *IEEE Transactions on Robotics*, vol. 26, no. 6, pp. 1006–1017, December 2010.

[25] M. E. Alshafeei, A. Hosney, A. Klingner, S. Misra, and I. S. M. Khalil, "Magnetic-based motion control of a helical robot using two synchronized rotating dipole fields," *5th IEEE RAS/EMBS International Conference on Biomedical Robotics and Biomechatronics (BioRob)*, pp. 151–156, August 2014.

[26] I. S. M. Khalil, B. E. Wissa, B. G. Salama, and S. Stramigioli, "Wireless motion control of paramagnetic microparticles using a magnetic-based robotic system with an open-configuration," *In Proceedings of the International Conference on Manipulation, Manufacturing and Measurement on the Nanoscale (3M Nano)*, pp. 190–196, October 2015.

[27] I. S. M. Khalil, A. Alfar, A. F. Tabak, A. Klingner, S. Stramigioli, and M. Sitti, "Positioning of drug carriers using permanent magnet-based robotic system in three-dimensional space," *In Proceedings of the IEEE International Conference on Advanced Intelligent Mechatronics (AIM)*, pp. 1117–1122, 2017.

[28] D. H. Kim, E. B. Steager, U. K. Cheang, D. Byun, and M. J. Kim, "A comparison of vision-based tracking schemes for control of microbiorobots," *Journal of Micromechanics and Microengineering*, vol. 20, no. 6, p. 065006, June 2010.

[29] I. S. M. Khalil, A. Adel, D. Mahdy, M. M. Michael, M. Mansour, N. Hamdi, , and S. Misra, "Localization and control of helical robots for clearing superficial blood clots," *APL Bioengineering*, January 2019. (Under Review).

[30] J. Hu, C. Chang, N. Tardella, J. English, and J. Pratt, "Effectiveness of haptic feedback in open surgery simulation and training systems," *Medicine Meets Virtual Reality*, vol. 119, pp. 213–218, February 2005.

[31] D. Prattichizzo, F. Chinello, C. Pacchierotti, and M. Malvezzi, "Towards wearability in fingertip haptics: a 3-dof wearable device for cutaneous force feedback," *IEEE Transactions on Haptics*, vol. 6, no. 4, pp. 506–516, October 2013.

[32] H. Kim, C. Seo, J. R. J. Lee, S. Yu, , and S. Lee, "Vibrotactile display for driving safety information," *in Proceedings of IEEE Intelligent Transportation Systems Conference*, pp. 573–577, October 2006.

[33] R. Traylor and H. Z. Tan, "Development of a wearable haptic display for situation awareness in altered-gravity environment: some initial findings," *in Proceedings of the IEEE Symposium on Haptic Interfaces for Virtual Environment and Teleoperator Systems*, pp. 159–164, February 2002.

[34] R. Sodhi, I. Poupyrev, M. Glisson, and A. Israr, "Aireal: Interactive tactile experiences in free air," *ACM Transactions on Graphics*, vol. 32, no. 4, pp. 506–516, July 2013.

[35] S. Gupta, D. Morris, S. N. Patel, and D. Tan, "Airwave: Noncontact haptic feedback using air vortex rings," *in Proceedings of ACM International Joint Conference on Pervasive and Ubiquitous Computing*, pp. 419–428, September 2013.

[36] T. Hoshi, M. Takahashi, T. Iwamoto, and H. Shinoda, "Noncontact tactile display based on radiation pressure of airborne ultrasound," *IEEE Transactions on Haptics*, vol. 3, no. 3, pp. 155–165, February 2010.

[37] B. Long, S. A. Seah, T. Carter, and S. Subramanian, "Rendering volumetric haptic shapes in mid-air using ultrasound," *ACM Transactions on Graphics*, vol. 33, no. 6, pp. 181(1–10), November 2014.

[38] M. Weiss, C. Wacharamanotham, S. Voelker, and J. Borchers, "Fingerux: near-surface haptic feedback on tabletops," *in Proceedings of the ACM Annual Symposium on User Interface Software and Technology*, pp. 615–620, October 2020.

[39] P. Berkelman, M. Miyasaka, and J. Anderson, "Co-located 3d graphic and haptic display using electromagnetic levitation," *in Proceedings of IEEE Haptics Symposium*, pp. 77–81, March 2012.

[40] A. Adel, M. A. Seif, G. Hoelzl, M. Kranz, S. Abdennadher, and I. S. M. Khalil, "Rendering 3d virtual objects in mid-air using controlled magnetic fields," *in Proceedings of the IEEE International Conference on Intelligent Robots and Systems (IROS)*, September 2017.

[41] A. Adel, M. M. Micheal, M. A. Seif, S. Abdennadher, and I. S. M. Khalil, "Rendering of volumetric shapes using an electromagnetic-based system," *in Proceedings of the IEEE International Conference on Intelligent Robots and Systems (IROS)*, October 2018.

[42] J. B. Brink, A. J. Petruska, D. E. Johnson, and J. J. Abbott, "Factors affecting the design of untethered magnetic haptic interfaces," *IEEE Haptics Symposium*, pp. 107–114, February 2014.

[43] A. Hosney, A. Klingner, S. Misra, and I. S. M. Khalil, "Propulsion and steering of helical magnetic microrobots using two synchronized rotating dipole fields in three-dimensional space," *in Proceedings of the IEEE International Conference on Intelligent Robots and Systems (IROS)*, pp. 1988–1993, September-October 2015.

[44] Y. Ma, S. Soatto, J. Kosecka, and S. S. Sastry, "An invitation to 3-d vision: from images to geometric models," *Springer-Verlag*, vol. 26, no. 1, March 2004.

[45] I. S. M. Khalil, A. F. Tabak, K.Sadek, D.Mahdy, N.Hamdi, and M. Sitti, "Rubbing against blood clots using helical robots: modeling and in vitro experimental validation," *IEEE Robotics and Automation Letters*, vol. 2, no. 2, pp. 927–934, April 2017.

[46] A. Hosney, J. Abdalla, I. S. Amin, N. Hamdi, and I. S. M. Khalil, "In vitro validation of clearing clogged vessels using microrobots," *in Proceedings of the IEEE RAS/EMBS International Conference on Biomedical Robotics and Biomechatronics (BioRob)*, pp. 272–277, June 2016.

[47] D. Mahdy, N. Hamdi, A. E. Sharkawy, S. Hesham, and I. S. M. Khalil, "The influence of mechanical rubbing on the dissolution of blood clots," *in Proceedings of the International Conference of the IEEE Engineering in Medicine and Biology Society (EMBC)*, July 2018.

[48] A. Adel, M. Mansour, M. M. Michael, A. Hassan, I. S. M. Khalil, and S. Misra, "Magnetic localization for and electromagnetic-based haptic interface," *IEEE Magnetics Letters*, 2019. (Under Review).

[49] X. Guo, G. Yan, and W. He, "A novel method of three-dimensional localization based on a neural network algorithm," *Journal of medical engineering and technology*, vol. 33, no. 3, pp. 192–198, 2009.

[50] A. J. Petruska and J. J. Abbott, "Optimal permanent-magnet geometries for dipole field approximation," *IEEE Transactions on Magnetics*, vol. 49, no. 2, pp. 811–819, February 2013.